A processive rotary mechanism couples substrate unfolding and proteolysis in the ClpXP degradation machinery

Zev A. Ripstein[1,2†], Siavash Vahidi[1,2,3,4†], Walid A. Houry[1,4], John L. Rubinstein[1,2,5] and Lewis E. Kay[1,2,3,4]

[1]Department of Biochemistry, University of Toronto, Toronto, Ontario, M5S 1A8, Canada.

[2]The Hospital for Sick Children Research Institute, Toronto, Ontario, M5G 0A4, Canada.

[3]Departments of Molecular Genetics, University of Toronto, Toronto, Ontario, M5S 1A8, Canada.

[4]Department of Chemistry, University of Toronto, Toronto, Ontario, M5S 3H6, Canada.

[5]Department of Medical Biophysics, University of Toronto, Toronto, Ontario, M5G 1L7, Canada.

† Z.A.R and S.V contributed equally to this work

Correspondence to: kay@pound.med.utoronto.ca; john.rubinstein@utoronto.ca

Abstract

The ClpXP degradation machine consists of a hexameric AAA+ unfoldase (ClpX) and a pair of heptameric serine protease rings (ClpP) that unfold, translocate, and subsequently degrade client proteins. ClpXP is an important target for drug development against infectious diseases. Although structures are available for isolated ClpX and ClpP rings, it remains unknown how symmetry mismatched ClpX and ClpP work in tandem for processive substrate translocation into the ClpP proteolytic chamber. Here we present cryo-EM structures of the substrate-bound ClpXP complex from *Neisseria meningitidis* at 2.3 to 3.3 Å resolution. The structures allow development of a model in which the cyclical hydrolysis of ATP is coupled to concerted motions of ClpX loops that lead to directional substrate translocation and ClpX rotation relative to ClpP. Our data add to the growing body of evidence that AAA+ molecular machines generate translocating forces by a common mechanism.

Introduction

Protein degradation plays a central role in cellular physiology, regulating the timing of cell division, controlling stress responses, and ensuring the timely removal of damaged or aberrantly folded proteins (1, 2). The ClpXP system is central to protein degradation in bacteria and mitochondria and is a key regulator of cellular homeostasis, pathogenesis, and intracellular parasitism (3–5). It also serves as a model for understanding the structure and function of other ATP-dependant proteolytic systems. The ClpXP holoenzyme is composed of a hexameric AAA+ (ATPases Associated with diverse cellular Activities) unfoldase (ClpX) and a tetradecameric serine protease consisting of two heptameric rings (ClpP). Together, the ClpXP complex acts to unfold and degrade protein substrates (Figure 1A) (6). ClpXP function is critical in many bacteria, and consequently small molecules that disrupt either the protease (e.g. β-lactones (7), phenyl esters (8, 9)) or AAA+ unfoldase (e.g. ecumicin (10), lassomycin (11), rufomycin (12), dihydrothiazepines (13)), or mimic the interaction between the two (e.g. acyldepsipeptides [ADEPs] (14–16)) can kill cells, establishing ClpXP as a target for novel therapeutics against a range of different infectious diseases and cancers (17–21).

X-ray crystallographic studies of ClpP alone reveal a barrel-like structure with the protease rings stacked coaxially to form an enclosed degradation chamber that sequesters the fourteen Ser-His-Asp catalytic triads (22, 23), akin to the 20S proteasome (24, 25). Early negative-stain electron microscopy showed that one or two ClpX particles can bind co-axially to ClpP, creating a continuous central channel for substrates from ClpX to the degradation chamber of ClpP (26–28). Biochemical and X-ray crystallographic studies show that the axial entrances to the degradation chamber are gated by flexible N-terminal loops of ClpP that open upon the binding of ClpX or ADEPs, allowing substrates into the degradation chamber (29–31). Binding

55 of ClpX and ClpP is mediated by loops containing an Ile-Gly-Phe motif (IGF loops) on ClpX
56 that dock into hydrophobic pockets on the apical interfaces of ClpP subunit pairs (32–34). N-
57 terminal loops on ClpP also transiently interact with ClpX (33, 35, 36). However, the precise
58 nature of these interactions and how they allow coordination of the activities of ClpX and ClpP
59 remains unclear.

60 ClpX uses energy released by ATP hydrolysis to create a pulling force that unravels
61 folded protein domains for translocation into the degradation chamber of ClpP (6). This
62 unfolding activity relies on a series of highly conserved loops in ClpX. These loops include the
63 'RKH' loops that surround the ClpX entrance pore and recognize substrates for proteolysis (37),
64 and a pair of "pore loops" in each protomer, termed pore-1 loop (GYVG motif) and pore-2 loop
65 (RDV motif) (Figure 1 – figure supplement 1A) that line the axial channel of the ClpX ring (38).
66 Bulky aromatic and aliphatic side chains of the pore loops transmit the pulling force to the
67 substrate, leading to its unfolding. The mechanism by which some AAA+ ATPases convert
68 energy from ATP hydrolysis into a mechanical force that unfolds substrates was established
69 recently (39–44), and structures of ClpP and ClpX in isolation have been determined (45–48).
70 However, the absence of structures showing ClpXP in the process of unfolding substrate has
71 prevented an understanding of the conformational changes that are necessary for substrate
72 engagement, unfolding, and translocation in this system. ClpXP must undergo hundreds of ATP
73 hydrolysis events to unfold and degrade a single protein, likely via a process involving
74 hydrolysis of one nucleotide at a time, but the lack of structural information for a ClpXP
75 holoenzyme has limited understanding of how unfolding and degradation are coupled. For
76 example, it is not clear how the symmetry mismatch (49–51) between the pseudo-symmetric

77 hexameric ClpX and the seven-fold symmetric ClpP affects both the binding and interaction of
78 these two components.

79 Here we present cryo-EM structures of the ClpXP holoenzyme from the gram-negative
80 pathogen *Neisseria meningitidis* engaged with a protein substrate. The ClpXP portion of the
81 structure is at 2.3 to 3.3 Å resolution, allowing construction of a nearly complete atomic model
82 of the complex. Our findings show how ClpX grips and translocates substrates into the
83 degradation chamber through a cycle of ATP hydrolysis events involving both concerted motions
84 of pore loops along the substrate, as well as motions of ClpX on the apical surface of ClpP. The
85 data lead to a model for interactions between symmetry-mismatched ClpX and ClpP that enable
86 continuous degradation of substrates as ClpX rotates relative to ClpP.

87

88 **Results**

89 **ATP-dependent binding and degradation of GFP-SsrA by ClpXP**

90 ClpX and ClpP from *N. meningitidis* were expressed separately in *E. coli* before purification with
91 metal affinity chromatography and size exclusion chromatography (SEC). Degradation assays
92 using green fluorescent protein bearing an eleven-residue SsrA tag (GFP-SsrA) (43) were
93 performed to ensure that the heterologously expressed *N. meningitidis* (Nm) ClpX and ClpP
94 proteins, when mixed, have the well-established activity of the ClpXP holoenzyme. The presence
95 of ClpP or ClpX alone led to no loss of GFP-SsrA fluorescence relative to background bleaching
96 in the GFP-alone control assay. ClpX, ClpP, and ATP were all necessary to degrade GFP-SsrA
97 (Figure 1B), confirming that degradation of GFP-SsrA by ClpXP is ATP-dependent. As shown
98 below and in previous work (33, 52–54), the presence of MgATP is required for tight binding
99 between ClpX and ClpP. Therefore, for further structural studies, an E185Q Walker B mutant of

100 NmClpX (ClpX-WB) was used to slow ATP hydrolysis and prolong the lifetime of the ClpXP
101 complex. SEC was performed to probe the oligomeric state of each component and the formation
102 of the holoenzyme, confirming that ClpP behaves as an oligomeric species, consistent with its
103 well-known tetradecameric architecture (Figure 1C – blue trace). ClpX-WB eluted as a hexamer
104 in the presence of 2 mM MgATP (Figure 1C – green trace). Incubation of ClpX-WB and ClpP in
105 the presence of MgATP resulted in a pair of higher molecular weight SEC peaks that contain
106 both ClpX and ClpP (Figure 1C – red trace and SDS-PAGE gel insert), presumably
107 corresponding to singly and doubly capped ClpXP complexes, showing that the *N. meningitidis*
108 ClpX:ClpP complex can be readily reconstituted *in vitro*.

109 To isolate a substrate-bound holoenzyme, ClpXP was incubated with GFP-SsrA in the
110 presence of MgATP. SEC fractions corresponding to doubly capped ClpXP bound to GFP-SsrA
111 (Figure 1–figure supplement 1B - denoted with a *) were applied to specimen grids and vitrified
112 for cryo-EM analysis. Visual inspection of the micrographs, as well as 2D classification of
113 particle images, showed doubly capped complexes (Figure 1-figure supplement 2). However, 2D
114 classification showed multiple classes where the two ClpX rings have lower density than the
115 ClpP region, and other classes with one ClpX ring having strong density and the other having
116 weak density. An *ab initio* 3D map showed ClpP along with strong density for one ClpX ring
117 and only weak and fragmented density for the other (Figure 1–figure supplement 2C). Inspection
118 of the map revealed that the ClpX ring is offset and tilted relative to the ClpP symmetry axis (Fig
119 1D, Video 1). The poor density for the second ClpX hexamer is likely due to a lack of correlation
120 between binding offsets of the two ClpX rings that leads to incoherent averaging of one of the
121 ClpX rings in the map. The map of the intact complex was refined to an overall resolution of 2.8
122 Å (Figure 1–figure supplement 2C), however the density for the better-resolved ClpX ring

123 remained fragmented. Further local refinement and classification in cryoSPARC (55) improved
124 the density for ClpX and revealed two distinct conformations, at 3.3 Å and 2.9 Å resolution
125 (Figure 1–figure supplement 2), hereafter referred to as Conformations A and B, respectively.
126 Focused refinement of ClpP with D7 symmetry enforced led to a map at 2.3 Å resolution (Figure
127 1–figure supplement 2).

128 **Overall architecture of NmClpXP**

129 Atomic models built into the cryo-EM maps showed that in both Conformations A and B, ClpX
130 is positioned with an offset and is tilted relative to the seven-fold symmetry axis of ClpP (Figure
131 1D, Video 1). Nevertheless, a continuous channel for substrate spans the ClpX and ClpP rings.
132 ClpP is in its active extended conformation (56), and closely resembles a published ADEP-bound
133 crystal structure with an all atom RMSD of 1.04 Å (56). Even though the full-length constructs
134 of ClpX included the zinc binding domains (residues 1-62), no density was found for these
135 domains in either conformation, likely due to their flexibility.

136 Conformations A and B of ClpX both contained additional density along their axial
137 channels, adjacent to the pore loops, likely from the GFP-SsrA substrate that co-eluted with
138 ClpXP from the SEC column (Figure 1E and 1F - orange) (Figure 1 – Figure Supplement 1B).
139 As the Walker B mutant has low unfolding activity (see below), the density observed likely
140 corresponds to the unstructured region of the degron tag. The substrate enters ClpX at an angle
141 of ~15° relative to the ClpP symmetry axis, and is gripped by five of the six ClpX protomers
142 arranged in a right-handed spiral, akin to other AAA+ ATPases in their substrate-bound
143 conformations (39–44). The sixth protomer forms a disengaged "seam" that bridges protomers at
144 the beginning and end of the spiral. In the description that follows we have labeled the protomers

145 X1 through X6 corresponding to their position in the spiral (Figure 1F), and consider the
146 configuration in which X1 is the disengaged "seam" protomer of Conformation A.

147 The main differences between Conformations A and B are within the protomer that
148 adopts the bridging seam position, and where the seam is located relative to ClpP. In
149 Conformation A, protomer X1 is disengaged from substrate and in the seam position (Figure 1F
150 left - dark blue) while in Conformation B protomer X6 is disengaged from substrate and in the
151 seam position (Figure 1F right - yellow). However, these two seam positions are not equivalent:
152 in Conformation A the seam is further from the apical surface of ClpP in what we designate as
153 the "upper seam" (US) position (Figure 1D,F - dark blue), while in Conformation B, the seam is
154 closer to ClpP in the "lower seam" (LS) position (Figure 1D,F - yellow).

155 **The symmetry-mismatched interaction interface between ClpX and ClpP**

156 ***ClpX IGF Loops:*** In both Conformations A and B of ClpXP, there is clear density for most of
157 the IGF loops that extend from the ClpX ring towards the apical surface of ClpP (Figure 2A). In
158 Conformation A, clear density is observed for only five of the six IGF loops, with weak density
159 belonging to the IGF loop of the X6 protomer (white dotted line in Figure 2B left; Figure 2-
160 figure supplement 1). In Conformation B, the density of the X6 IGF loop is significantly stronger
161 than in Conformation A, so that all six of the IGF loops are accounted for (residues 264-274,
162 Figure 2B, right; Figure 2C; Figure 2-figure supplement 1), with the loops binding six of the
163 seven pockets on ClpP. In both Conformations A and B, the empty ClpP binding pocket is
164 located between the X5 and X6 protomers of ClpX (Figure 2B). The lack of density for the IGF
165 loop belonging to protomer X6 in Conformation A (Figure 2-figure supplement 1) is likely due
166 to conformational flexibility and sub-stoichiometric binding of this IGF loop into the ClpP
167 binding pocket.

168 All six IGF loops in ClpX adopt different configurations in Conformations A and B
169 (Figure 2-figure supplement 1). The ClpX residues immediately following where the IGF loops
170 contact ClpP (residues 275-280) show weak or no density, likely indicating flexibility. This
171 property allows the IGF loops to accommodate movement of the ClpX protomers relative to
172 ClpP (Figure 2D-F), analogous to a set of springs. For instance, in Conformation A the X1
173 protomer is closer to the ClpP surface than in Conformation B and its IGF loop is thus compact
174 in this state. In contrast, in Conformation B the loop is fully extended, allowing the X1 protomer
175 to reach ~7 Å towards the top of the spiral to engage the substrate (Figure 2F; Figure 2-figure
176 supplement 1). In this way the flexibility of the IGF loops accommodates the spiral arrangement
177 of ClpX necessary to bind and unfold substrate, while maintaining contact with the planar ring of
178 ClpP. Additionally, the IGF loops allow the X2 protomer to move laterally away from the ClpP
179 pore while the X4 and X5 protomers move toward it to form a structure in which the ClpP and
180 ClpX rings are displaced with respect to each other (Figure 2D-red arrow; Figure 2E).
181 ***ClpP N-terminal Gates:*** Degradation assays (31, 35, 57–59) show that ClpX allows substrate
182 access to the degradation chamber of ClpP, suggesting that ClpX binding opens the N-terminal
183 gates of ClpP. Indeed, in both Conformations A and B the gates are in the "up" state, forming
184 ordered β-hairpins (Figure 2G; Figure 2-figure supplement 2). These β-hairpins closely resemble
185 the conformation seen in the ADEP-bound structures of NmClpP (56) and are notably different
186 from the disordered conformations observed in NmClpP when it is not bound to either ClpX or
187 ADEP (Figure 2–figure supplement 2B). By forming ordered gates, ClpX binding creates a wide
188 entrance pore with a diameter of ~23 Å for substrates to pass through into the ClpP degradation
189 chamber (Figure 2G, left; Figure 2–figure supplement 2). While it has long been suspected that

190 the activating mechanism of ADEPs involves a disorder-to-order transition of these gates (30),
191 this observation provides direct evidence that ClpX binding has the same effect.

192 In both Conformations A and B, the rigidification of the ClpP N-terminal gates varies
193 substantially between protomers. At one extreme, the N-terminal residues of the ClpP protomer
194 that is not bound to an IGF loop have the weakest density, appearing to possess the most
195 flexibility at the top of the β-hairpin (Figure 2G center; Figure 2-figure supplement 2E). In
196 contrast, the N-terminal residues of the ClpP protomer proximal to the X5 ClpX protomer, are
197 held rigidly through contacts with the ATPase (Figure 2G right). This interaction is mediated by
198 a pair of α-helices from protomer X5 (residues 254-262 and 291-296) adjacent to the IGF loop,
199 and by another X5 α-helix that precedes the pore-2 loop (residues 186-192). The three α-helices
200 stabilize the β-hairpin structure of the ClpP N-terminal residues by interacting with Arg17 at the
201 top of the hairpin (Figure 2E inset). These interactions are unique for the X5 protomer due to the
202 lateral displacement of the ClpX ring relative to the axial pore of ClpP (Figure 2A), with the X2
203 protomer shifted furthest from the pore while the X5 protomer is pulled overtop of the pore
204 (Figure 2D and F). Even without interacting directly with ClpX, the remaining five ClpP
205 protomers have nearly rigid N-terminal gates, with reduced density only for residues located in
206 the turn of the β-hairpin that likely reflects increased flexibility in this region (Figure 2-figure
207 supplement 2F). Gate rigidification therefore appears to be mediated by an allosteric effect when
208 IGF loops engage their respective ClpP binding pockets, akin to the effect observed upon ADEP
209 binding (15, 30). In the ClpXP complex with substrate bound, only a single ClpX protomer (X5)
210 interacts directly with a single ClpP gate at any given time. The mechanism of substrate
211 translocation described below involves movement of the ClpX ring on the apical surface of ClpP,
212 with each ClpX protomer forming contacts with a ClpP gate as translocation proceeds.

213 **Substrate Engagement by ClpX**

214 ClpX fits neatly into the emerging consensus for how AAA+ unfoldases engage substrate (39–
215 43). In both Conformations A and B, five of the six pore-1 loops of ClpX interact tightly with the
216 substrate backbone, with Tyr153 forming the majority of the interface (Figure 3A and B). These
217 protomers generate a right-handed spiral that wraps around an 8 to 10 residue stretch of the
218 substrate along the central channel of ClpX (Figure 3C and D). In Conformation A, the X1 pore-
219 1 loop in the US orientation is disengaged, with the X2 protomer at the top of the spiral. As the
220 spiral continues downwards, protomers X3, X4, and X5 make contacts with the substrate. The
221 spiral terminates with the X6 pore-1 loop that is engaged with the substrate closest to the ClpP
222 apical surface (Figure 3C). In Conformation B, the X6 pore-1 loop is disengaged (LS
223 orientation), while the X1 pore-1 loop engages a new section of substrate (Figure 3D) and the X5
224 protomer is now located closest to the ClpP surface. When transitioning between substrate-
225 engaged and disengaged states, the X6 pore-1 loop undergoes a large conformational change
226 (Figure 3E). As it disengages the substrate the "lasso" fold (Figure 3E, left) that allows Tyr153
227 and Val154 of pore 1 to point towards the substrate is replaced by a short α-helix immediately
228 following the GYVG motif of the loop.

229 Interestingly, the X1 and X5 protomers make additional contacts with the substrate in
230 Conformation B. Whereas all of the pore-2 loops from the other five protomers are radially
231 removed and disengaged from the substrate, the X1 protomer extends its pore-2 loop residues
232 Ile198 and Thr199 to engage the substrate at a position three or four residues down the substrate
233 chain from where its pore-1 loop binds (Figure 3D and F). The RKH loops, located at the top of
234 the ClpX ring (Figure 3–figure supplement 1), are highly conserved motifs among the ClpX
235 family of AAA+ unfoldases and are known to contribute to substrate recognition (60–62). In

236 Conformation B only the RKH loop of X5 directly engages substrate, with its His230 residue
237 interacting at a position three or four residues up the substrate chain from where its pore-1 loop
238 binds (Figure 3D and F). In order to contact substrate at this position the RKH loop of the X5
239 protomer rearranges to point toward ClpP (Figure 3F), in contrast to the other RKH loops that
240 point away from the axial channel of ClpX (Figure 3-figure supplement 1). These five RKH
241 loops are located away from the substrate, and have weaker density in the maps, likely indicating
242 flexibility.
243
244 **Nucleotide State and Cycling in ClpX**
245 The cryo-EM maps allowed unambiguous identification of the nucleotide bound to each ClpX
246 protomer. In Conformation A, there is strong density for ATP and a magnesium cofactor in
247 protomers X2, X3, X4, and X5, while the X1 and X6 protomers are ADP loaded, with no density
248 for either the γ-phosphate or magnesium (Figure 4A,4C). As in both the classic and HCLR clades
249 of AAA+ ATPases (39–43), the orientation between the large and the small AAA+ domains of
250 ClpX changes considerably depending on the nucleotide state. In Conformation A, both the X1
251 and X6 protomers adopt conformations that allow the X1 protomer to move away from the pore
252 in the US position (Figure 4-figure supplement 1) and there is reduced surface area buried
253 between X1 and its neighboring protomers X2 and X6. In agreement with this finding, the local
254 resolution in the cryo-EM maps (Figure 4-figure supplement 2) suggests that the X1 protomer in
255 the US position is significantly more flexible than the other protomers. In Conformation B only
256 the X6 protomer is ADP-bound. The X1, X2, X3, X4, and X5 protomers are ATP-bound with
257 clear density for the γ-phosphate and the magnesium cofactor (Fig 4B and D). Interestingly, the
258 X5 protomer adopts a unique orientation between its large domain and small domain compared

259 to the other ATP-bound protomers in order to accommodate the translation of the X6 protomer
260 away from the substrate translocation channel into the LS position (Figure 4B orange box; Figure
261 4-figure supplement 1).

262 In Conformation A, the β- and γ-phosphates of the bound ATP are stabilized by
263 interactions with the sensor-II arginine (Arg369) of the same subunit and the arginine finger
264 (Arg306) from the adjacent clockwise protomer (Figure 4C). In the ADP-bound sites of the X1
265 and X6 protomers, both arginines have moved away, allowing for a more open nucleotide
266 binding pocket (Figure 4C). In Conformation B both the sensor-II arginine and the arginine
267 finger contact the β and γ-phosphates in only four of the five ATP-bound protomers (X1, X2,
268 X3, and X4) (Figure 4D). In the X5 protomer (at the bottom of the spiral), the adjacent X6
269 protomer and its arginine finger have pivoted away from the nucleotide into the LS position,
270 allowing the sensor-II arginine to move closer to the γ-phosphate of the bound nucleotide. While
271 there is clear density for the γ-phosphate, the resolution of our experimental map was not
272 sufficient to differentiate between ATP and a long-lived post hydrolysis ADP/P_i state. Notably,
273 this key sensor II-priming motif in the nucleotide site adjacent to an ADP bound site has also
274 been reported for the Lon protease bound to substrate (42), a close relative in the HCLR clade of
275 AAA+ proteins.

276 The arrangement of nucleotides in our map suggests that substrate-bound ClpX
277 hydrolyzes ATP in a sequential manner, contrary to previous reports that ATP hydrolysis by
278 ClpX is a stochastic process (63). To test these models of ATP hydrolysis we quantified the GFP
279 degradation rates of ClpX that were doped with varying fractions, F_{WB}, of catalytically-impaired
280 E185Q Walker B ClpX protomers (Figure 5). The exact composition and population of resulting
281 complexes can be calculated using combinatorial statistics, as described previously (43, 64, 65).

282 If ATP hydrolysis and substrate translocation were stochastic, the activity of each protomer
283 would be independent of others in the ClpX hexamer. Consequently, in the stochastic model, the
284 expected outcome of introducing Walker B protomers into a WT ClpX hexamer would be a
285 linear decrease in activity as the ratio of Walker B mutants incorporated randomly into the
286 complex increases (Figure 5B – green line). However, GFP degradation rates drop sharply as the
287 Walker B ratio increases (Figure 5B – blue circles), closely following the $y = (1 - F_{WB})^6$ curve
288 that shows the fraction of ClpX complexes remaining fully WT at each F_{WB} mixing ratio (Figure
289 5B – red line). This outcome is expected only for a strictly sequential model of substrate
290 translocation where a single catalytically-impaired protomer blocks the unfolding activity of an
291 entire ClpX hexamer. It is inconsistent with the previous stochastic model that predicts that
292 unfolding and translocation are possible with just a single active subunit.
293

294 **Discussion**

295 In this study we used cryo-EM to build atomic models of a ClpXP complex bound to a SsrA-
296 tagged GFP substrate. Structures of a variety of different AAA+ rings with substrates have
297 emerged in the past several years (39–43), providing a description of how these ATP-dependent
298 molecular machines unfold substrates. In addition, methyl-TROSY NMR studies of a VAT-
299 substrate complex provided atomic-level insights into structural changes associated with the
300 substrate as it is pulled into the lumen of the unfoldase (66). Nevertheless, a detailed
301 understanding of how a pair of symmetry mismatched ClpP/ClpX rings can work in tandem to
302 unfold, translocate, and subsequently degrade substrate in a processive manner has remained
303 elusive. Our structural data suggest a translocation mechanism that can be explained in terms of a
304 pair of conformers, denoted as Conformations A and B here, that represent two steps along the

305 substrate translocation pathway (Figure 6A). To aid in the following discussion we have color-
306 coded the ClpX protomers and refer to them with their X1 - X6 labels. As we will discuss, each
307 of these protomers will cycle between all six protomer positions along the spiral, including,
308 among others, a state primed to hydrolyze ATP (denoted as ATP*) as well as the LS and US
309 positions. This cycling is linked to ATP hydrolysis, to the attachment position of ClpX pore-
310 loops along the substrate, and to the interaction of ClpX IGF loops with ClpP. We begin our
311 discussion of the unfolding/translocation cycle with the X1 protomer in Conformation A in the
312 US position, detached from substrate and bridging the lowest and highest positions of the ClpX
313 spiral. Both X1 and X6 protomers are ADP-bound, while the remaining protomers are in ATP-
314 bound states. In Conformation B, X1 moves to the highest position of the spiral with respect to
315 substrate (compare Figure 2F, top and bottom panels) simultaneously exchanging ADP for ATP
316 in its nucleotide binding pocket (Figure 6B). This transition brings X1 into close proximity with
317 X2 and allows engagement of X1's pore loops with substrate. The X1 pore-l loop now sits at the
318 top of the spiral, two substrate residues above the X2 pore loop (Figure 6A and B), thereby
319 translocating additional residues of substrate into the unfoldase. This transition also leads to
320 release of substrate by X6, which pivots away from the central pore to adopt the LS position
321 (second ring, Figure 6A). ATP hydrolysis and phosphate release by X5, which was in the ATP-
322 hydrolysis primed ATP* state, restores the ClpX spiral back to the Conformation A state, (third
323 ring of the four in Figure 6A), with X6 now assuming the US position. The complex is thus reset
324 so that it can take another step along the substrate during the next A to B transition (third ring to
325 fourth ring in Figure 6A). The cumulative effect of these transitions is a cycling of ClpX
326 protomers through different positions on the spiral (Figure 6A and B). For example, the protomer
327 initially in the US position (X1 in our discussion) will, with each step, move along the spiral

328 such that it transitions from the US position to the top of the spiral (Conformation B) and then
329 successively moving to lower spiral positions, through the ATP* state and finally the LS
330 position, as substrate is translocated. Each Conformation A→Conformation B→Conformation A
331 step results in the exchange of ADP for ATP and a single ATP hydrolysis event. Continuous
332 repetition of these steps leads to a processive "hand-over-hand" translocation of substrate
333 through the axial pore of ClpX into ClpP (Illustrated in Video 2).

334 The sequential hydrolysis of ATP at the ATP* position results in unidirectional substrate
335 translocation and movement of pore loops along the substrate (Figure 6B), with the counter
336 clockwise hydrolysis cycle translating into a repeated downward pulling force on the substrate.
337 Both the sequential hydrolysis of ATP as well as the "hand-over-hand" substrate pulling model
338 appear to be conserved for AAA+ unfoldases (39–43).

339 The cycle described above, in which each protomer eventually adopts all positions in the
340 spiral, has implications for how the IGF loops interact with the ClpP binding pockets. If the
341 spiral position of each ClpX protomer was independent of IGF binding, alignment of the
342 asymmetric ClpX spiral would lead to averaging of the IGF loops into all the pockets of ClpP
343 during cryo-EM map refinement. However, our structures clearly show an empty IGF pocket on
344 ClpP *only* between the ATP* and LS positions of Conformation B (Figure 2B), suggesting that
345 this pocket must undergo a "cycle" as well (Figure 6C). Thus, following ATP hydrolysis and
346 phosphate release, the IGF loop of the protomer in the ATP* position (X5 initially) must leave
347 its engaged pocket and move to bind the adjacent empty site on ClpP (red arrows in Figure 6C),
348 as the complex transitions back to Conformation A (third ring in Figure 6A). In this state, the
349 IGF loop appears not to have assumed a structure that allows for tight binding as only weak
350 density is observed for it in EM maps. In contrast, strong binding is observed for this loop in

351 Conformation B (Figure 4-figure supplement 1). Consistent with this model, the IGF loop of the
352 X5 protomer has an "extended/stretched" structure in the ATP* position of Conformation B
353 (Figure 2F), which likely causes strain and facilitates loop release and subsequent binding to the
354 corresponding site on the adjacent ClpP protomer (Figure 6C). After seven IGF loop release and
355 reengagement events, accompanied by seven ATP hydrolysis steps, the 'empty' ClpP binding
356 site makes a complete cycle, returning to its starting position (Figure 6C). The accompanying
357 motion of ClpX on the apical surface of ClpP for a given IGF loop transition is complex and
358 subtle, yet seven of these transitions lead to a net 60° rotation of ClpX with respect to ClpP (note
359 the positions of the purple ClpX protomer in the first and seventh panels in Figure 6D; Video 3).
360 The model described above is the simplest one that is consistent with our data. More complicated
361 models can be envisioned that require additional states for which we have no experimental data.

362 During preparation of this manuscript two manuscript preprints reported structures of
363 ClpXP from *L. monocytogenes* (67) and from *E. coli* (68), with ClpX resolutions ranging from
364 3.9 to 6 Å. While density maps and atomic models are not available for direct comparison with
365 the NmClpXP, a few important similarities and differences are notable. In all species, the ClpX
366 ring appears to adopt a similar offset relative to the symmetry axis of ClpP, indicating that the
367 general architecture of the ClpXP machinery is conserved. Notably, however, the N-terminal
368 apical loops of *L. monocytogenes* ClpP are not rigidified upon ClpX binding (67), in contrast to
369 the observation here that the gates rigidify upon binding to create a pore for substrate entry. In
370 the case of *L. monocytogenes* ClpXP, unusual head-to-head dimers were observed that appeared
371 to be mediated by the zinc binding domains. Despite the presence of the zinc binding domains in
372 our *N. meningitidis* construct, no such dimers were observed. While this difference may be due
373 to differences across species, we note that the glutaraldehyde chemical crosslinker used to

374 stabilize the *L. monocytogenes* ClpXP complex may have induced the formation of artefactual
375 dimers.

376 Notably, substrate engagement is different between the ClpXP from *N. meningitidis*
377 described here and from *E. coli* (68). In the Conformation A seen with *N. meningitidis*, there is
378 no engagement of substrate by any of the six pore-2 or six RKH loops, while in Conformation B
379 only a single RKH loop and a single pore-2 loop contact substrate (Figure 3D and F). This
380 observation is in contrast to the recently reported *E. coli* ClpXP structures (68) in which
381 arginines located in the pore-2 loop from three to five different protomers (depending on the
382 structure), as well as multiple RKH loops, form major contacts with substrate. The differences in
383 these interactions may reflect the fact that while pore-1 loop and RKH loop motifs are critical for
384 forming interactions with substrate, and in the case of pore-1 loops in particular, in providing the
385 force for translocation, additional contacts may differ between species and may be necessary for
386 recognition of degradation signals and for substrate specificity. The RKH loops are essential for
387 the recognition of SsrA-tagged substrates by *E. coli* ClpX, while human ClpX, which lacks RKH
388 loops but contains pore-1 loops with the same sequence as *E. coli* ClpX, fails to recognize
389 substrates with the SsrA-tag. Notably, however, an engineered human construct bearing the pore-
390 2 and RKH loops of *E. coli* ClpX is able to unfold SsrA-tagged substrates (61). Electrostatic
391 interactions appear to play a critical role in substrate recognition by the positively charged RKH
392 loop. For example, AKH and RAH mutants that reduce the positive charge of the RKH motif
393 weaken the affinity of *E. coli* ClpX for the negatively charged α-carboxylate of the SsrA tag
394 while increasing its affinity for the positively charged λO and MuA degradation tags (61).
395 Reordering of RKH loop residues to KHR and KRH results in significantly impaired substrate
396 degradation (68) and a more disrupting AAA mutant does not support ClpP degradation of a

397 SsrA-tagged substrate (68). Furthermore, the single point mutation RKH to RKA results in loss
398 of activity for both SsrA and λO tagged substrates. The tight contact between H230 and the
399 substrate in our maps provides a structural basis for understanding these mutagenesis results."

400 Although in the ClpXP structures from *E. coli* (68) the ClpX ring adopts the same spiral
401 staircase arrangement observed in many AAA+ ATPases (39–43, 69, 70), strongly supporting
402 the "hand-over-hand" mechanism of substrate translocation, the authors of this work instead
403 posit a stochastic mechanism (63, 68) for the HCLR clade of ATPases based on the observation
404 of only a single bound ADP in their structures. In the stochastic model only a single protomer
405 pulls the substrate, via a state that has yet to be observed. Such a model, involving stochastic
406 nucleotide hydrolysis, appears inconsistent with the observations here, with those for the related
407 Lon protease (42) where two neighbouring protomers are bound with ADP, and with a recent
408 structural model for a substrate-bound *E. coli* ClpAP complex showing that the unbinding and
409 rebinding of flexible IGL loops is coupled to substrate translocation as each protomer makes its
410 way from the bottom to the top of the spiral (71). The proposed mechanism in that case is similar
411 to the one suggested here for *N. meningitides* ClpXP. The stochastic model is also in conflict
412 with functional studies presented in this manuscript and for the VAT AAA+ unfoldase (43)
413 whereby nucleotide hydrolysis was shown to occur in a cycle that could be disrupted through the
414 substitution of a single hydrolysis-impaired protomer into the ATPase ring. In contrast, the
415 identification of two conformations in the *N. meningitidis* enzyme and observations of the bound
416 nucleotides in each ClpX protomer leads to a simple model of cyclic hydrolysis that, in turn,
417 results in unidirectional substrate translocation. In this model, the substrate is always gripped by
418 multiple protomers, with only a single protomer disengaged as it traverses from the bottom to the
419 top of the spiral. While unique features will undoubtedly continue to emerge regarding subtle

420 functional aspects of different AAA+ unfoldases it is likely that the translocating forces
421 generated by these molecular machines are based on a common mechanism.

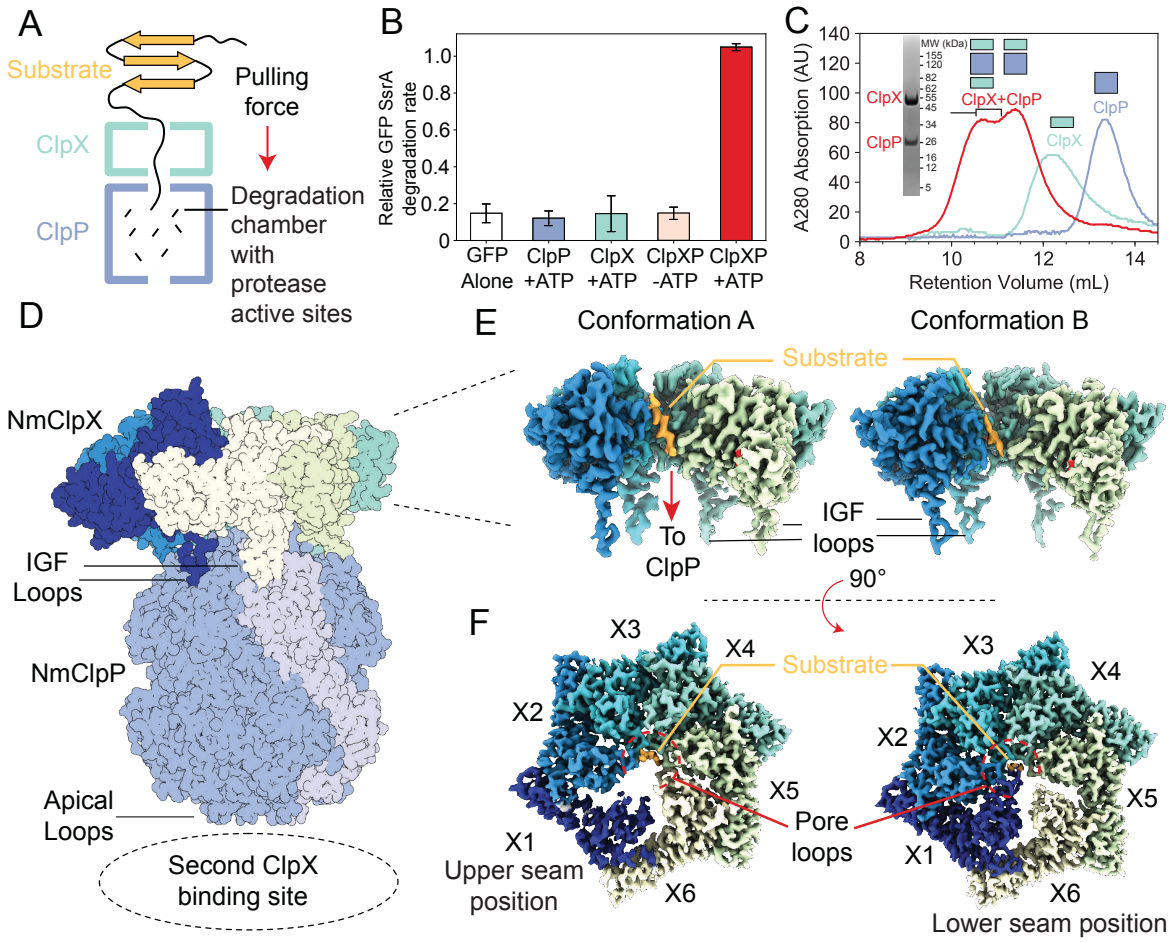

Figure 1. Functional and structural characterization of ClpXP from *N. meningitidis*. (A) Schematic representation of the ClpXP degradation machinery. The overall positions of the substrate (orange), ClpX unfoldase (green), and the ClpP protease (blue) are shown; (B) GFP-SsrA degradation by ClpXP is ATP-dependant. The degradation rate of GFP-SsrA is monitored by measuring loss of fluorescence. The components (ClpX, ClpP, ATP) included for each measurement are denoted on the plot. All measurements included GFP-SsrA and were performed in triplicate on WT ClpXP; (C) ClpXP complex formation monitored by size exclusion chromatography (SEC). SEC profiles of isolated ClpP (blue trace) and ClpX (green trace) are consistent with their expected molecular weights. SEC profile of a 2:1 $ClpX_6$:$ClpP_{14}$ mixture (red trace) incubated for 10 minutes in the presence of MgATP shows the formation of doubly- and singly-capped ClpXP complexes. The running buffer for all traces contained 2 mM MgATP. SDS-PAGE gel of SEC fractions shows that they contain both ClpP and ClpX; (D) Overall architecture of the ClpXP complex as established by cryo-EM. The ClpP double ring component is shown in dark blue, with the exception of a pair of opposing protomers shown in light blue shade to delineate the IGF loop binding site that is located at the interface between protomers. Cutaway side (E) and top (F) views of Conformations A and B of ClpX resulting from focused classification and local refinement. The IGF loops that bind to ClpP, and the presence of substrate (orange) in the axial channel of ClpX, are highlighted. Each of the ClpX protomers is labeled. In panel (F), the engagement of the substrate (orange) with five of the six pore loops is indicated (red semi-circle).

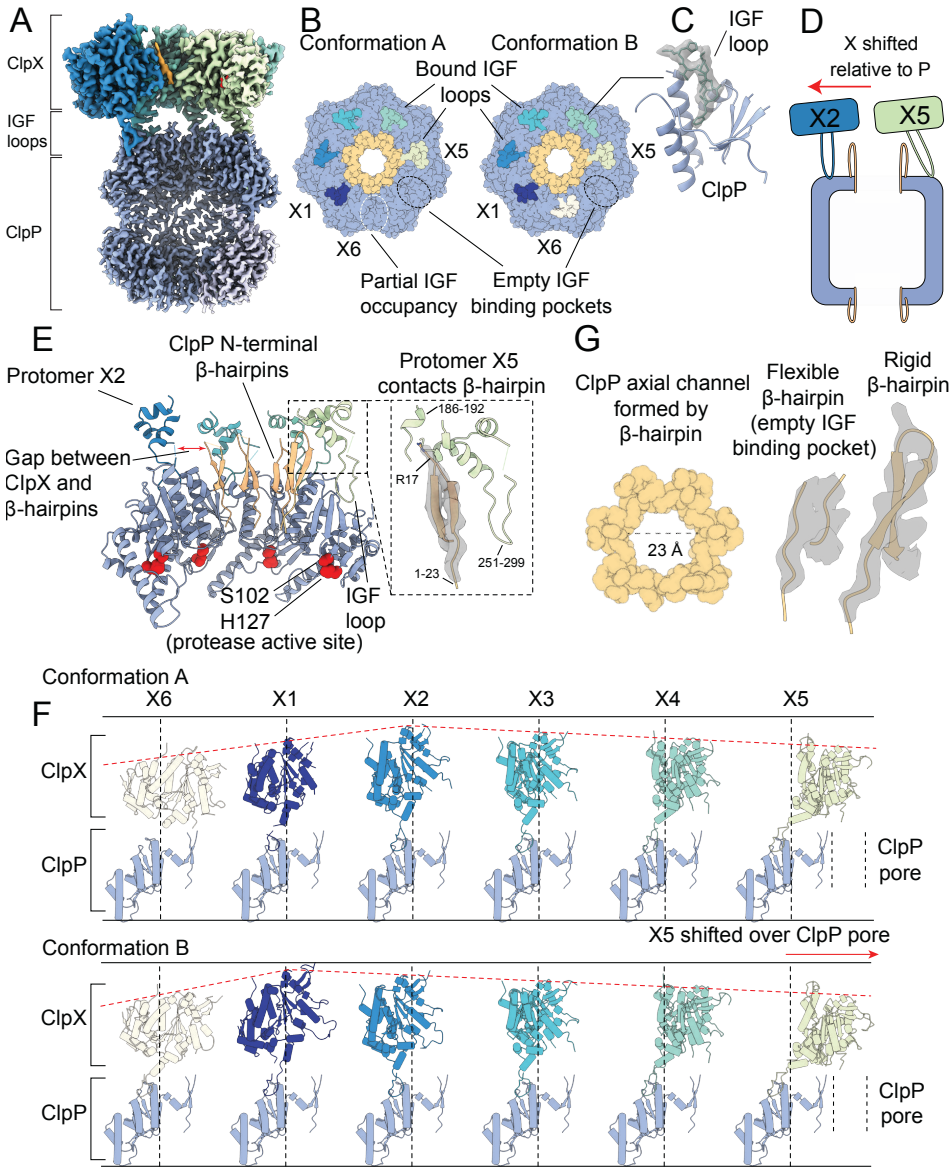

Figure 2: The interaction interface between ClpX and ClpP. Protomer X1 occupies the US position in Conformation A and protomer X6 the LS position in Conformation B. (A) Cutaway density map of the overall architecture of the ClpXP interaction interface. (B) Models for the ClpP apical surface and the ClpX IGF loops (residues 265-275). The empty IGF binding pocket (dotted oval) resides clockwise to the X5 protomer in both conformations. In Conformation A an IGF loop was not built into the map for protomer X6 due to weak loop density (yellow dotted line). (C) Model in map fit for an IGF loop (grey), surrounded by regions of ClpP comprising the IGF binding site (blue). (D) Interaction of the ClpP N-terminal gates with ClpX. The X2 protomer moves away from the gates, while the X5 protomer directly contacts the gate of the ClpP protomer to which its IGF loop is bound, shown schematically in (E). Inset shows the details of this interaction, with model in map fit for the ClpP β-hairpin. (F) Positions of ClpX protomers relative to ClpP. Images were generated by fitting all ClpP protomers to a common protomer and displaying the corresponding ClpX protomer. In both conformations ClpX adopts a spiral arrangement relative to ClpP (dotted red line). In Conformation A, the X2 protomer is located at the top of the spiral, while in Conformation B the X1 protomer occupies the top position, ~7 Å higher than its position in Conformation A. The ClpX protomers rotate and translate relative to ClpP; protomers X2 and X3 sit nearly atop their ClpP protomers, while X4 and especially X5 show large deviations from this position (vertical lines), with X5 sitting overtop the ClpP axial pore. (G) View down the channel formed by the N-terminal ClpP β-hairpins (left); density and models for the most flexible and rigid β-hairpins (center & right, respectively).

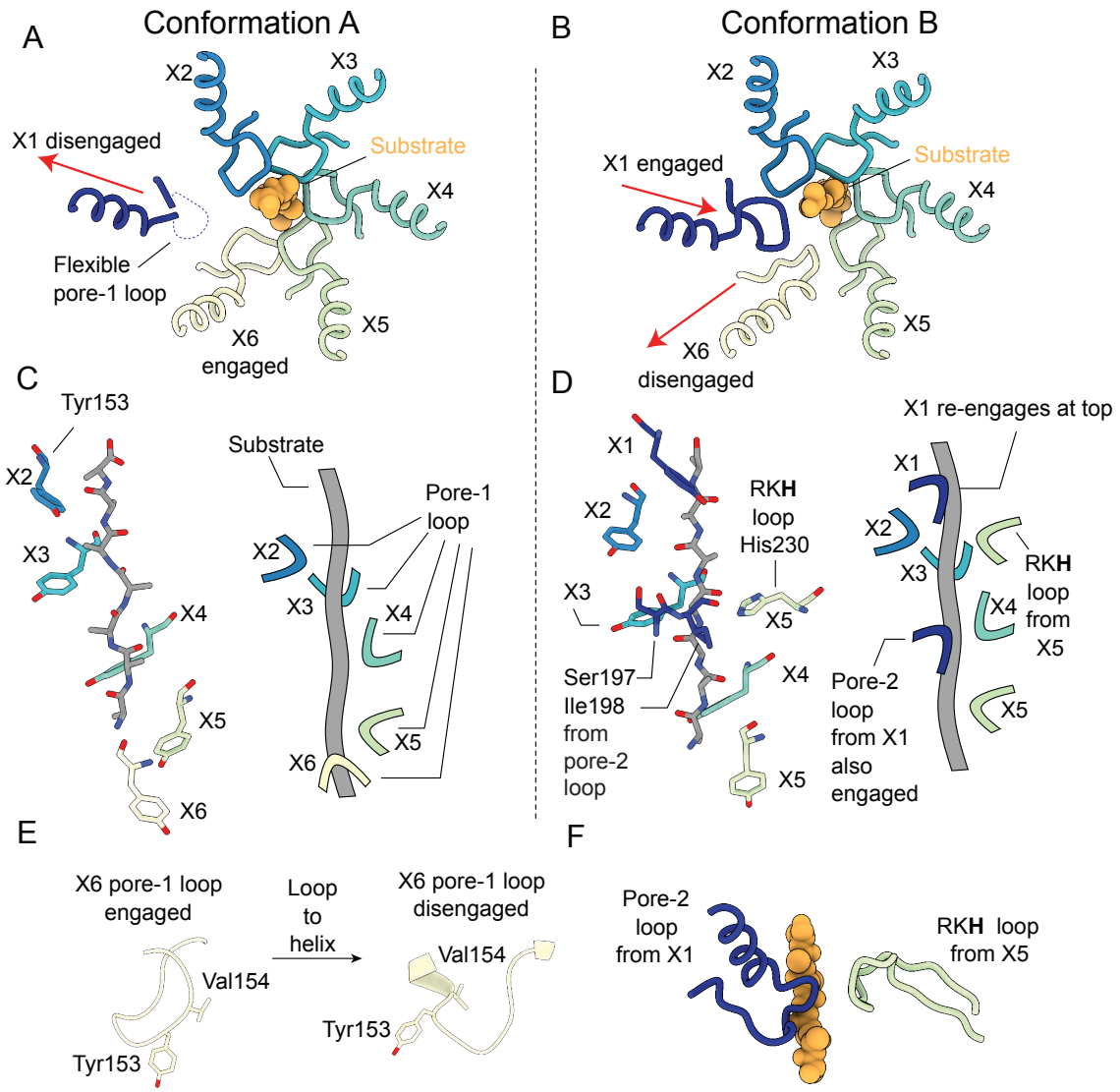

Figure 3. Substrate engagement by the ClpX pore loops. (A and B) Pore-1 loop residues grip the substrate, as observed in this view looking down the axial channel. The substrate is modelled as poly-Ala. (A) In Conformation A, the X1 protomer is disengaged from the substrate in the US position (red arrow) and shows noticeable flexibility in its pore-1 loop. (B) In Conformation B the X1 protomer contacts the substrate but the X6 protomer has disengaged into the LS position (red arrows). (C and D) Model of substrate and interacting residues, along with schematic, viewed perpendicular to the axial channel. (C) In Conformation A only the Tyr153 residue of the pore-1 loop makes significant contacts with the substrate; the 5 protomers (X2, X3, X4, X5, X6) form a downward spiral surrounding the backbone of the substrate chain, extending to the apical surface of ClpP. (D) In Conformation B, in addition to the five Tyr153 residues from the 5 gripping protomers (X1, X2, X3, X4, X5), more contacts are formed: Ser197 and Ile198 from the pore-2 loop of the X1 protomer and His230 from the RKH loop of the X5 protomer. (E) Substrate induced conformational changes of the X6 pore-1 loop upon releasing client. When the X6 protomer is substrate engaged its pore-1 loop forms a lasso like conformation, with Tyr153 and Val154 both pointing towards the axial channel (left). When disengaged, a part of the pore-1 loop becomes an α-helix, with Val154 and Tyr153 no longer pointing outwards (right). (F) Architecture of the additional contacts made by the pore-2 and RKH loops from the X1 and X5 protomers, respectively.

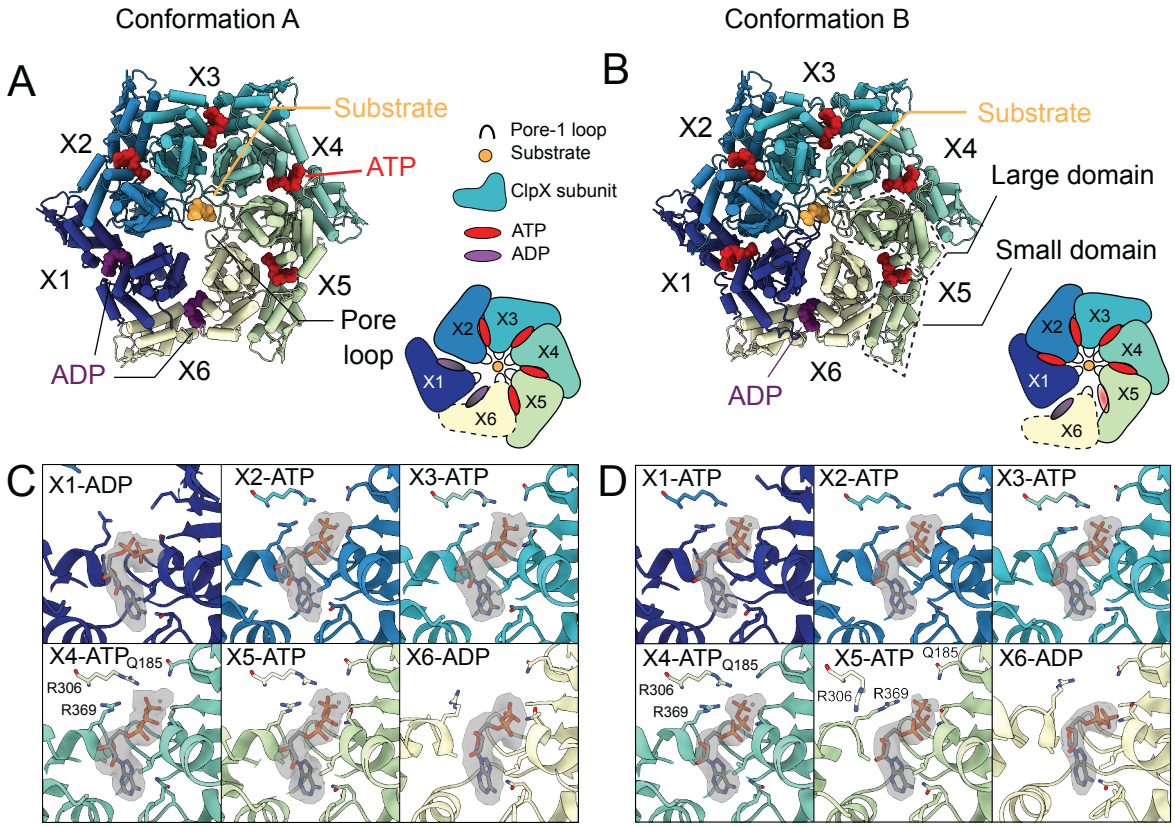

Figure 4. Nucleotide occupancy and interactions with ClpX. (A&B) Model of ClpX in conformations A and B, looking into the ClpX pore. Nucleotides are shown and color-coded, with ATP red and ADP purple, and bind between the large and small domains (boxed). Inset shows a schematic of the protomer positions and nucleotide occupancies. Conformation A has two bound ADP, in the X1 (dark blue, US in Conformation A in this representation) and X6 (yellow, LS in Conformation B in this representation) protomers, with the X1 protomer disengaged from the substrate and away from the axial pore (US position). In Conformation B only a single ADP is bound, protomer X1 is reengaged with substrate and X6 has disengaged. (C) Nucleotide binding sites of Conformation A, with key interacting residues shown along with the experimental density maps corresponding to bound nucleotide. In the ADP bound sites, both the arginine finger (R306) and the sensor-II arginine (R369) have moved away, while in the ATP bound sites they form close contacts with the β and γ-phosphates. (D) Nucleotide binding in Conformation B. As in Conformation A, R306 and R369 have moved away from the ADP, while in the X5 protomer only the arginine finger has moved away, while the sensor-II transitions closer to the γ-phosphate.

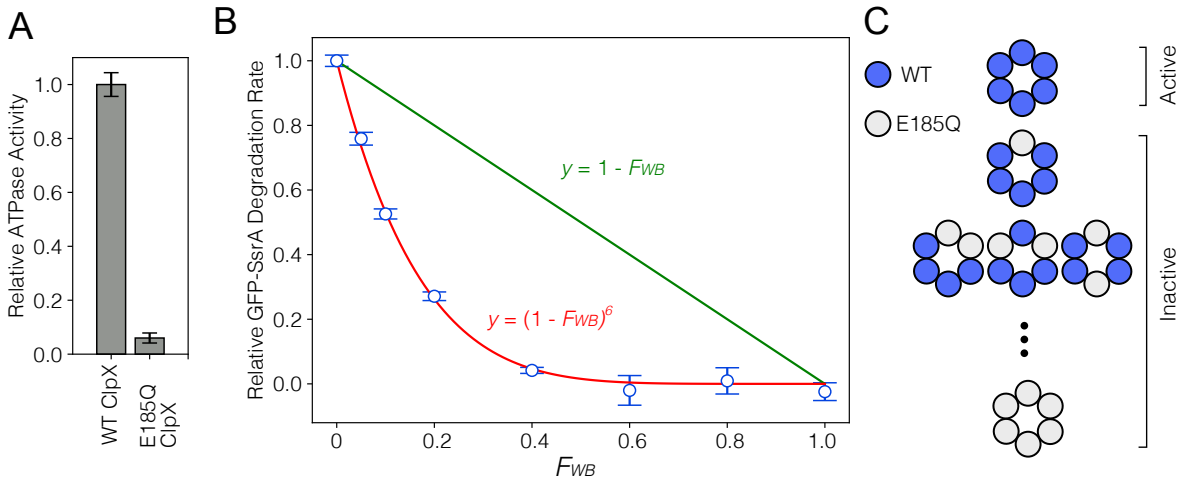

Figure 5. A single defective ClpX protomer derails function. (A) ATPase rates for WT ClpX and the E185Q ClpX Walker B mutant. Hydrolysis of ATP was measured with an enzyme-coupled assay (72). (B) GFP degradation rates monitored by the decrease in fluorescence signal as a function of the fraction of added E185Q ClpX protomers to hexameric ClpX, F_{WB} ([E185Q ClpX]/([E185Q ClpX] + [WT ClpX])). ClpX protomers bearing the slowly-hydrolyzing E185Q Walker B mutant were mixed with WT protomers at various ratios, F_{WB}, between 5-100% of the total protomer ClpX concentration. The activity decreases rapidly with increasing E185Q content, and closely follows the theoretical curve $y = (1 - F_{WB})^6$ that predicts the activity profile for the case where incorporation of one or more WB ClpX promoters is sufficient to abrogate function, as is predicted from our proposed translocation model. This curve (red) corresponds to the expected activity if only hexamers with six WT subunits contribute to GFP degradation while any complex with one or more E185Q mutants incorporated is functionally inactive. This observation contrasts the expected linear decrease (green line) for a stochastic model. (C) Schematic of the molecules produced via mixing.

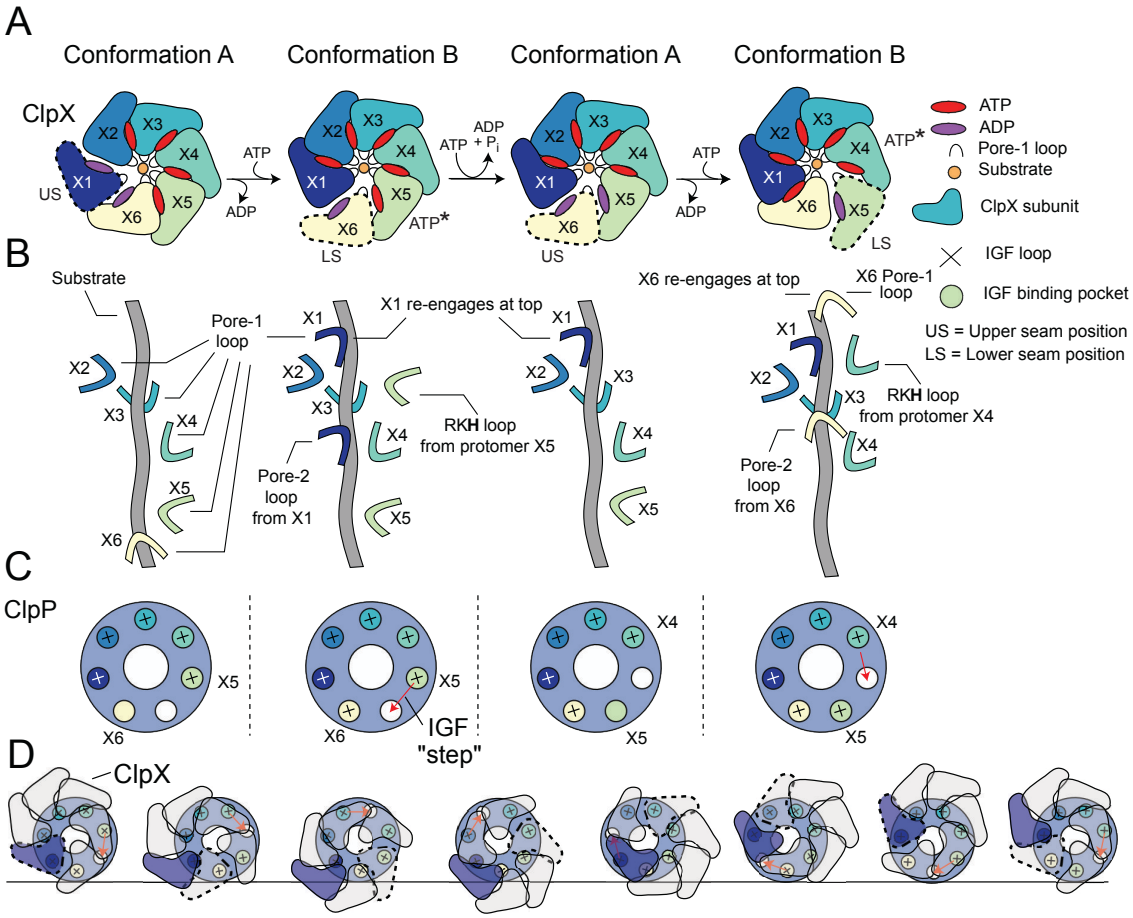

Figure 6. Translocation model for ClpXP. (A) Schematic of the ClpX nucleotide dependent conformational cycle. The transition from Conformation A to Conformation B is mediated through nucleotide exchange in the US position (1st to 2nd ring), with ATP hydrolysis and phosphate release in the ATP* position restoring the A conformation from the B state (2nd to 3rd ring) so that the cycle can repeat. In the new Conformation A (3rd ring), protomer X6 (yellow) adopts the US conformation and the X1 protomer (previous US) moves to the top of the spiral. In this way each protomer of the complex cycles through all positions as ATP is hydrolyzes in successively new ATP* protomer states, requiring the hydrolysis of seven ATPs. (B) Hand-over-hand mechanism of pore-loop mediated translocation. In the first A to B transition depicted in (A) X1 (US protomer) reengages at the top of the spiral and the LS pore 1 loop (X6 in Conformation B) disengages from the bottom of the spiral. As this is repeated the pore loops move "up" the substrate and pull it into the degradation chamber. (C) IGF loop movements accompanying the hand-over-hand movements of ClpX. Shown in the small circles are the seven IGF loop binding sites in ClpP with a '+' sign indicating engagement with an IGF loop of a given ClpX protomer. The binding sites are color coded according to the color of the protomer that interacts with the corresponding site. In conformation A, the IGF loop of X6 is unbound or only weakly bound, while in Conformation B it is bound. A new Conformation A is generated when the IGF loop from the ATP* protomer unbinds. It subsequently reengages with ClpP in a new Conformation B (third and fourth rings in Figure 5A). In this way the IGF loops "step" around the ClpP ring, with each complete rotation requiring the hydrolysis of seven ATPs. (D) Schematic of the ClpX-ClpP interactions during seven ATP hydrolysis steps that lead to a net rotation of ClpX protomers by 60º. Because of the six- to seven-fold symmetry mismatch a total of forty-two ATPs must be hydrolyzed to return the protomers back to their original starting positions in the cycle (*i.e.*, ring 1). Each of the seven ring structures corresponds to Conformation A, with the red arrows indicating the subsequent step of the IGF loop of the ATP* protomer along the cycle. The US protomer in each step is highlighted by the dashed trace.

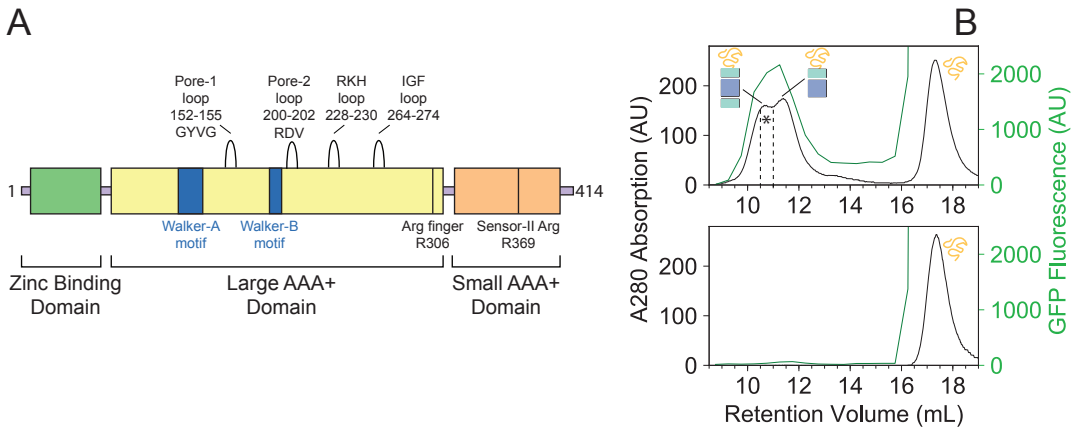

Figure 1 - Figure Supplement 1. (A) NmClpX primary sequence domain map. Important structural and functional motifs are denoted. (B) NmClpXP binds a SsrA-tagged GFP. SEC profiles for ClpXP incubated with GFP-SsrA (top panel) and GFP-SsrA alone (bottom panel) measured using absorbance at 280 nm (black trace) and GFP fluorescence (green trace - λ_{ex}:480nm, λ_{em}:508 nm). The region used for SDS PAGE analysis is highlighted by * (Figure 1C).

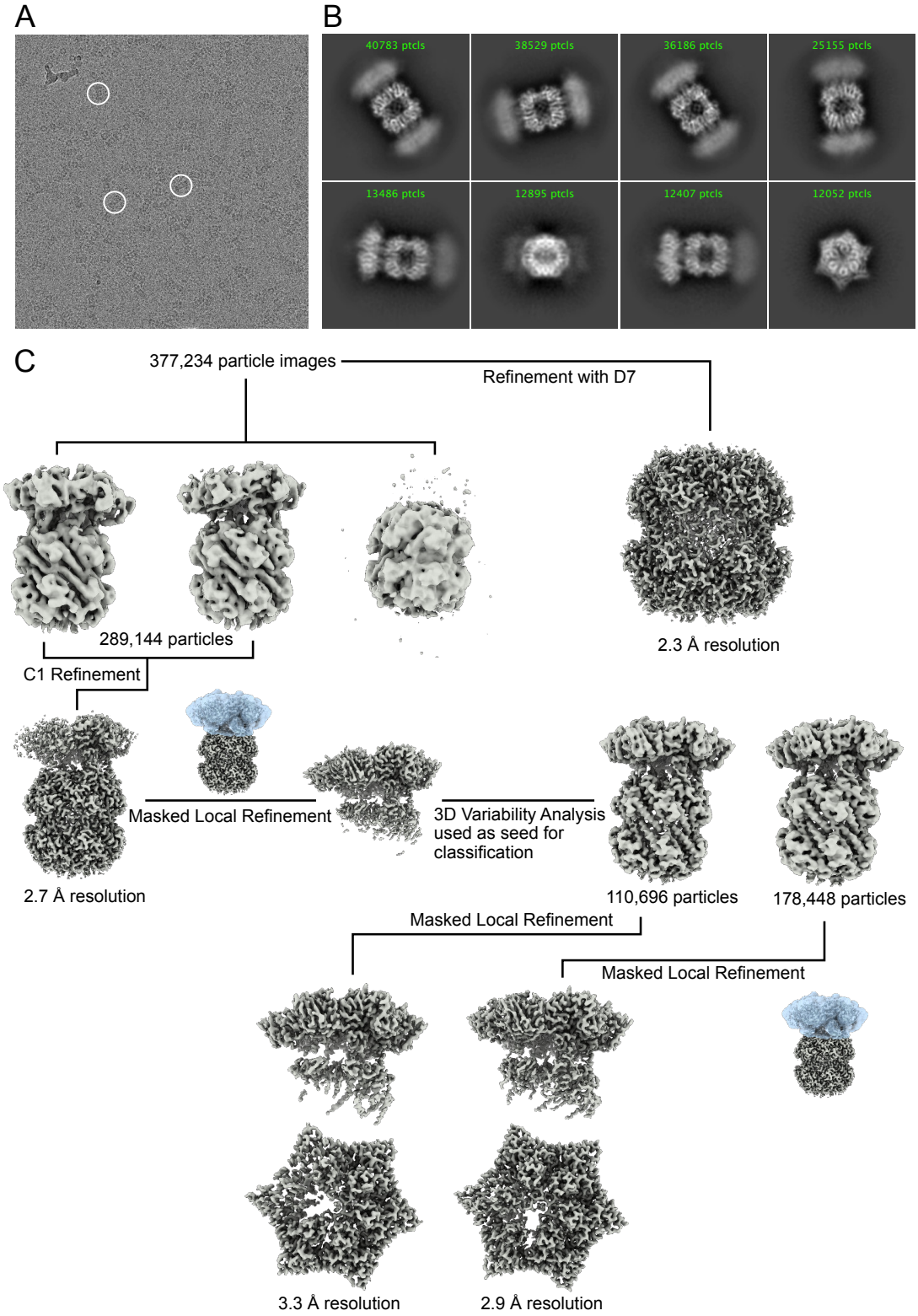

Figure 1 – Figure Supplement 2. Cryo-EM image processing. (A) Representative cryo-EM micrograph of NmClpXP bound to GFP-SsrA. Example complexes are circled in white. (B) Representative 2D class averages of NmClpXP with GFP-SsrA. (C) Image processing workflow used to obtain final maps.

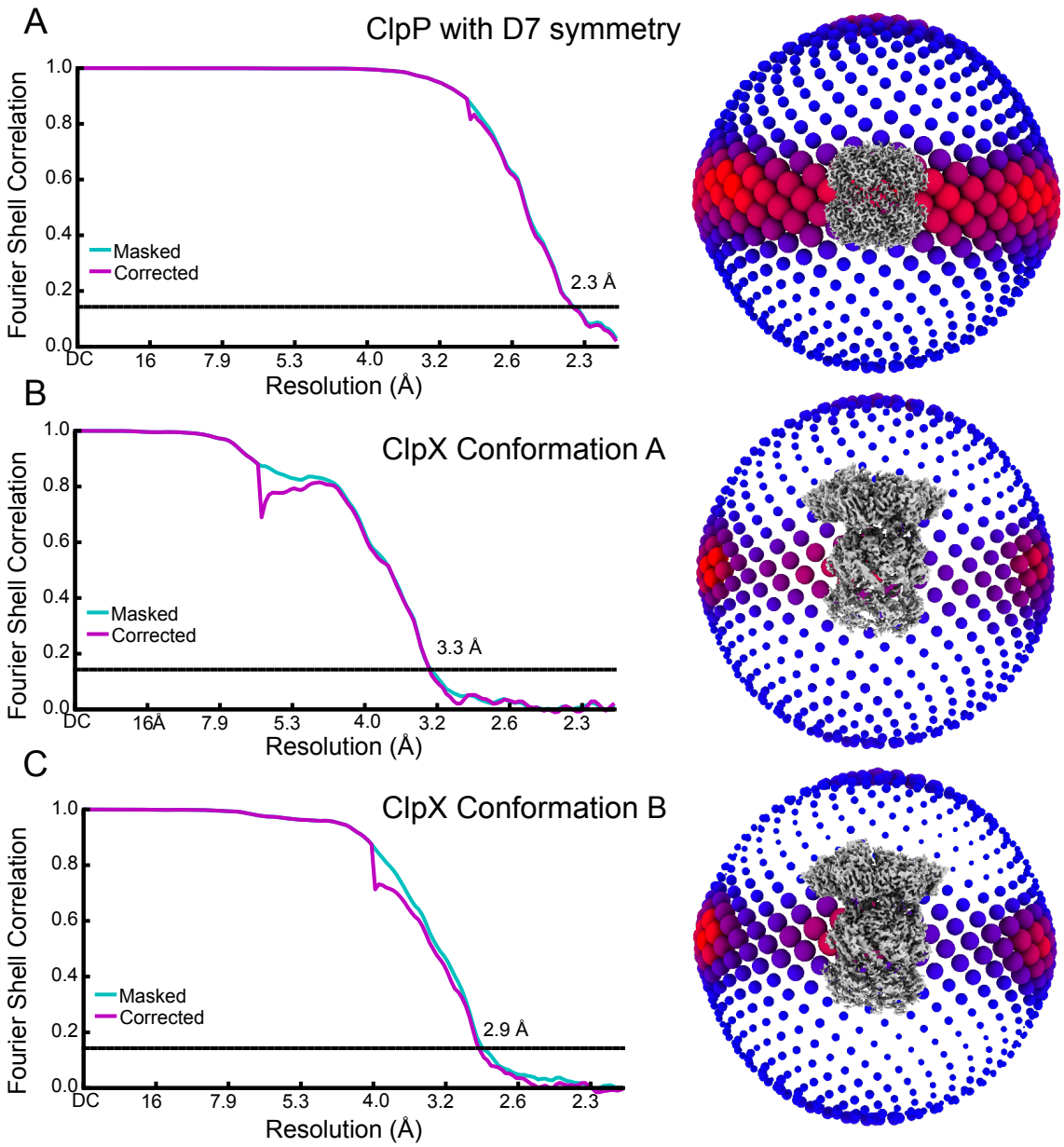

Figure 1 – Figure Supplement 3. Cryo-EM map validation. (A to C) Fourier Shell Correlation (FSC) plots (left) and orientation distribution (right). Resolution values reported are for FSC=0.143.

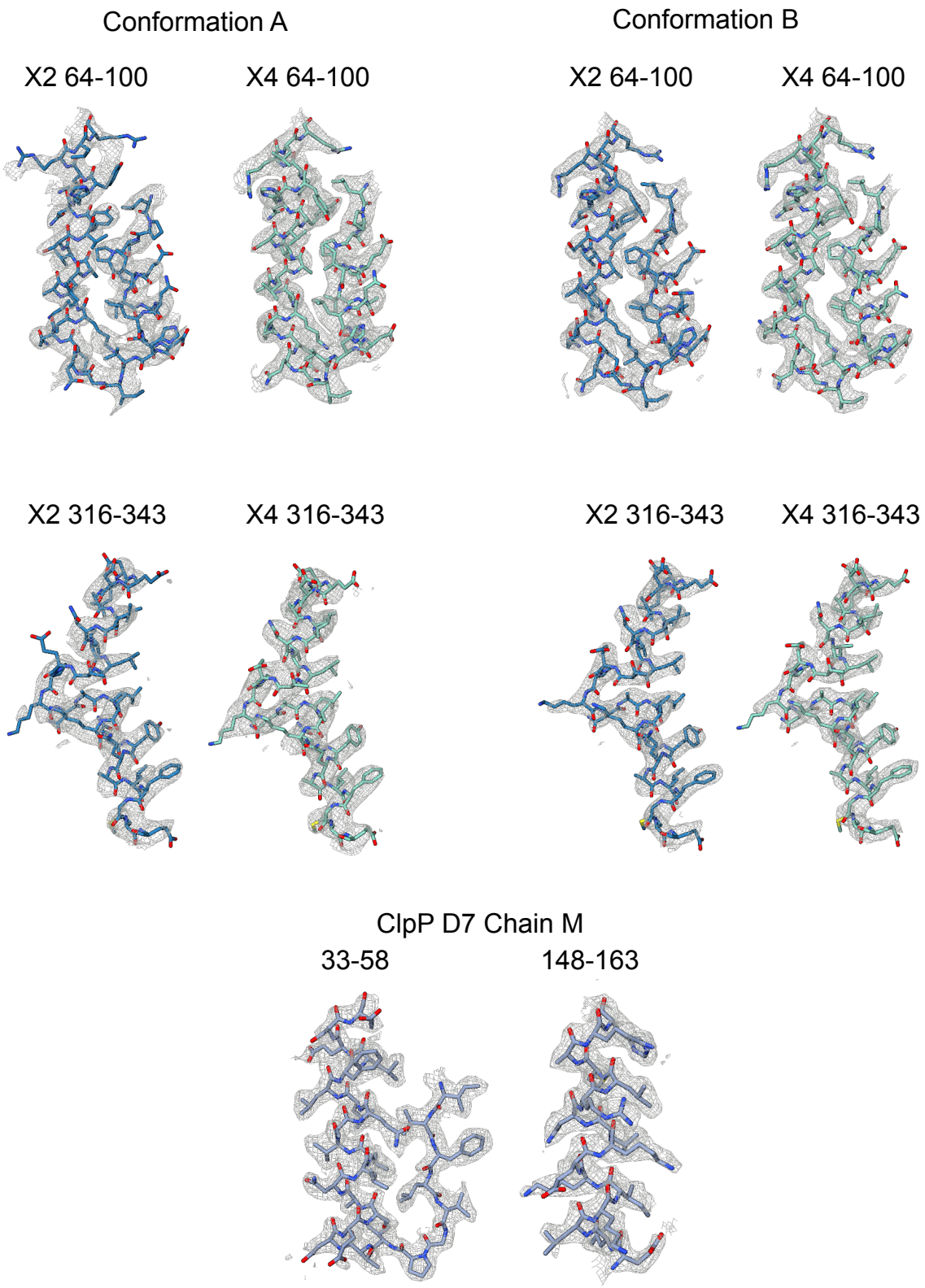

Figure 1 – Figure Supplement 4. Examples of regions of the atomic models built into the experimental cryo-EM maps.

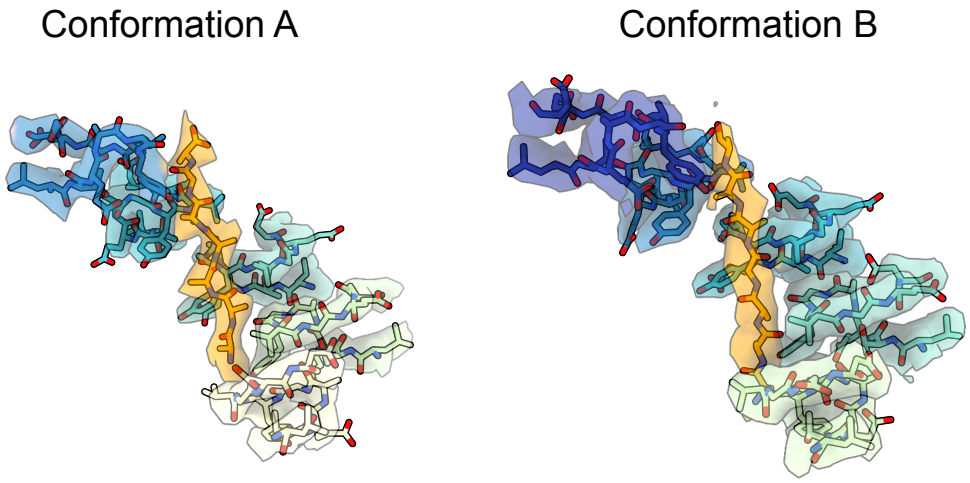

Figure 1 – Figure Supplement 5. Experimental density maps and models for the substrate pore-1 loop interaction interface.

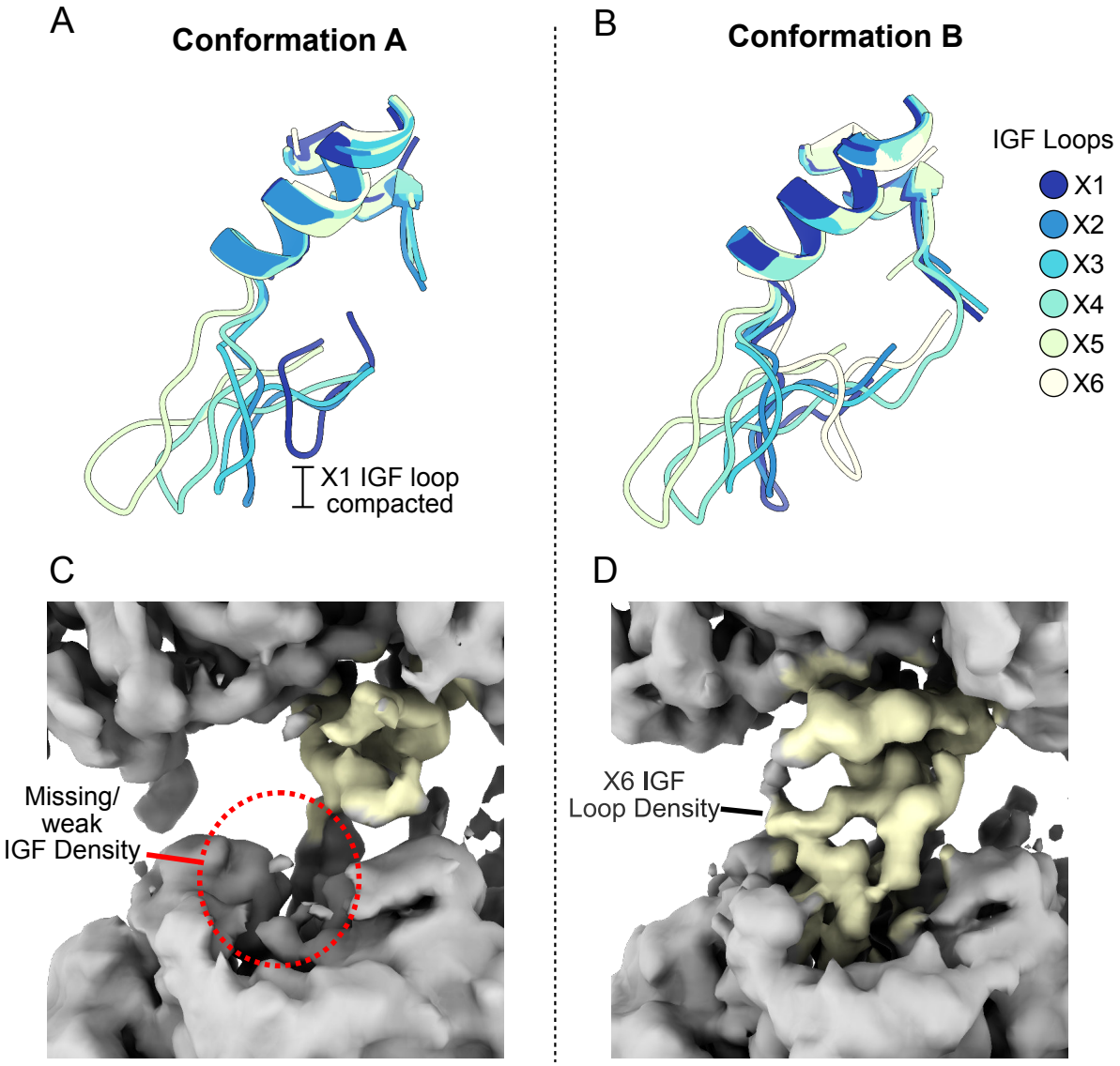

Figure 2 - Figure Supplement 1. IGF loop flexibility. (A and B) Large domains of ClpX were aligned and models for the IGF loops are shown. (C and D) Unsharpened density map for Conformations A and B looking at protomer X6.

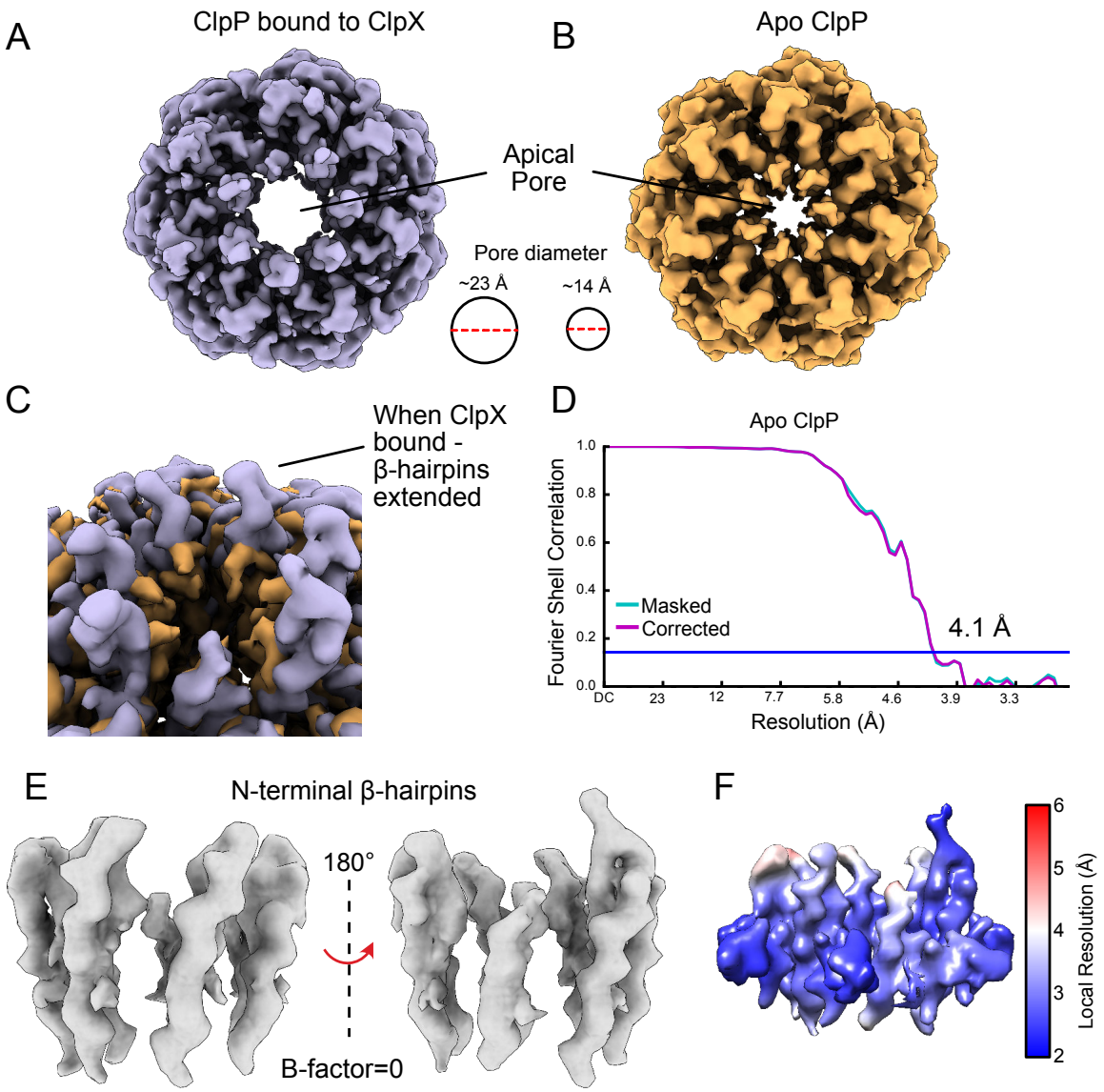

Figure 2 - Figure Supplement 2. The ClpP apical loops extend upwards from the ring surface. (A) Unsharpened density map of the ClpP N-terminal β-hairpins when bound to ClpX. (B) Cryo-EM map of apo ClpP from *N. meningitidis* showing that the apical loops no longer extend "up". (C) ClpX-bound and apo forms of ClpP overlaid. There is no noticeable density for the turn of the ClpP N-terminal β-hairpin in the apo form, and the β-hairpins point inwards, constricting the axial pore of ClpP. (D) Fourier Shell Correlation (FSC) plot for Apo-NmClpP. (E) Closeup view of the N-terminal β-hairpins when bound to ClpX. (F) Density map of the β-hairpins in the ClpXP complex, colored by local resolution.

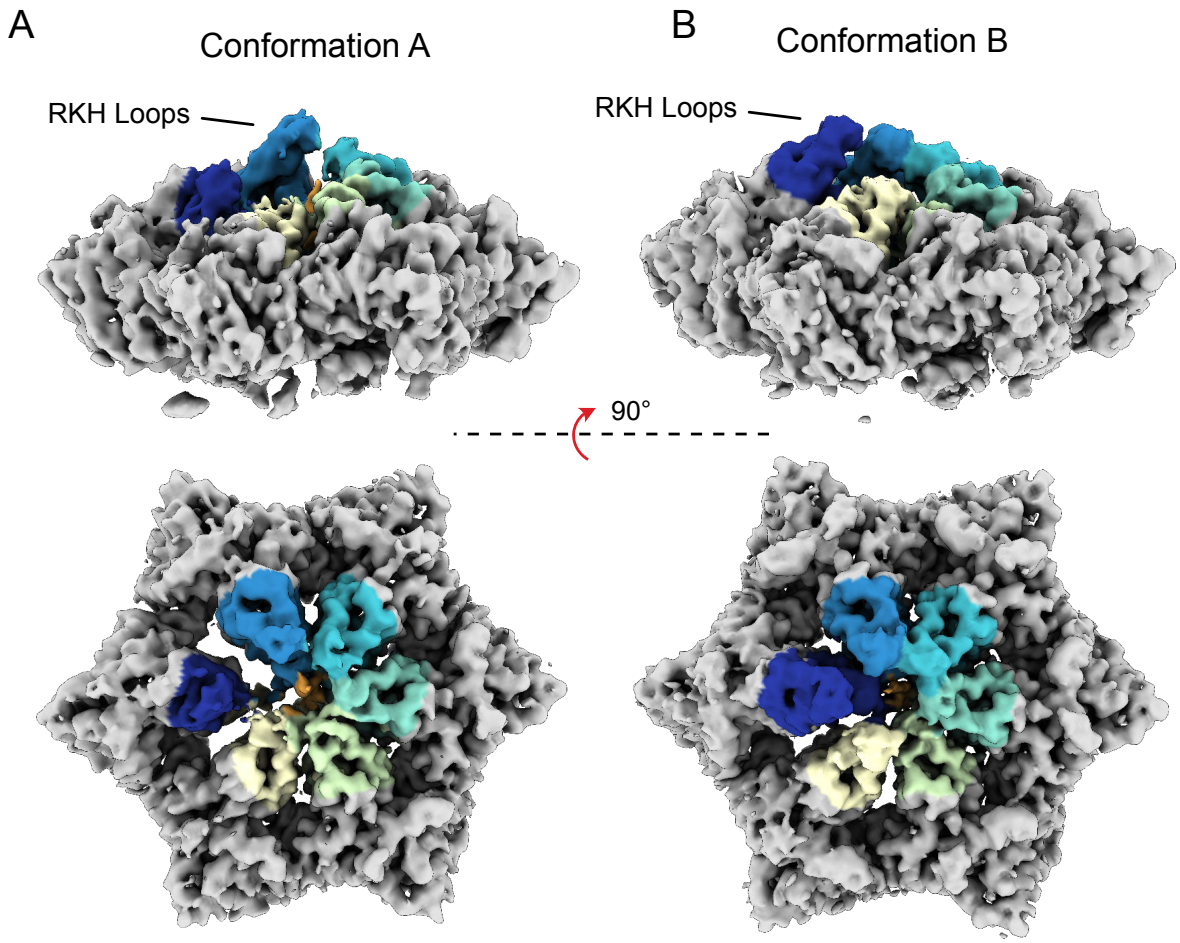

Figure 3 - Figure Supplement 1. RKH loop positions. (A and B) Unsharpened maps for both conformations A and B of ClpX are shown, with RKH loops highlighted in color (coloring done by a radius of 10 Å around residues 220-240).

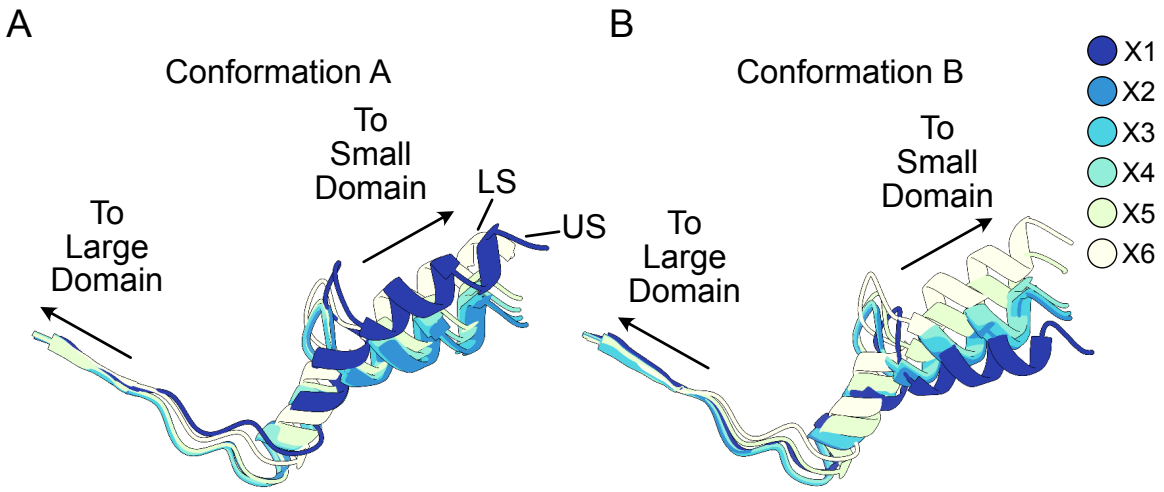

Figure 4 - Figure Supplement 1. Relative orientation between large and small domains of ClpX. (A and B). Residues 308-343 are shown. Note that protomers X1 and X6 in Conformations A and B, respectively, are displaced from substrate. These show among the largest differences in domain orientations.

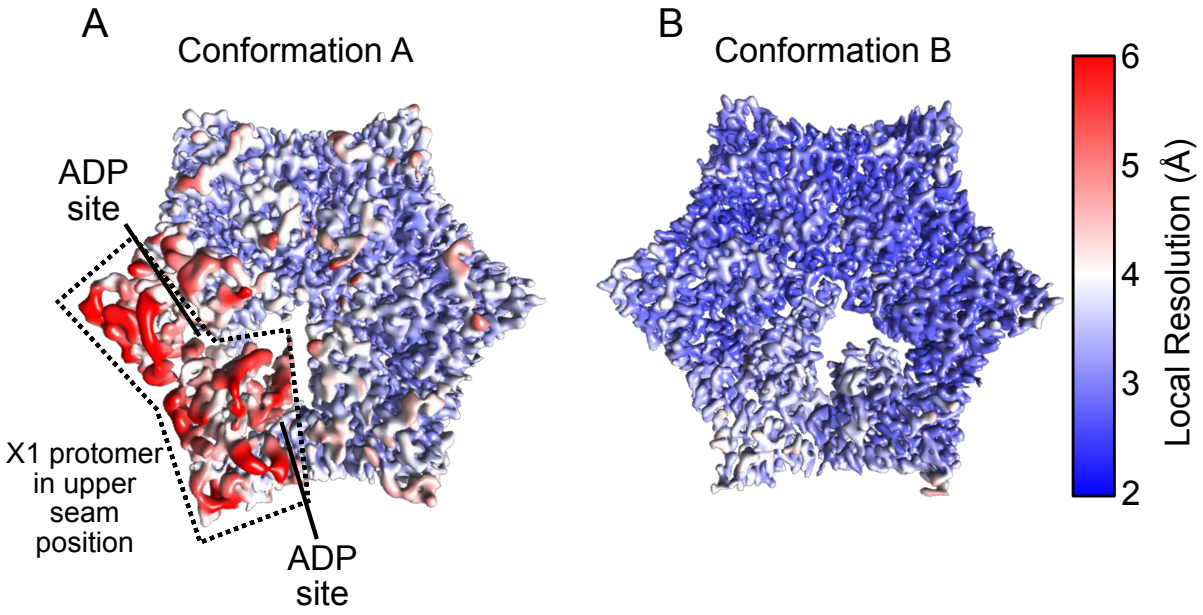

Figure 4 - Figure Supplement 2. Local resolution maps of ClpX. (A and B) Density maps colored by local resolution for Conformations A and B. In Conformation A the US protomer is highlighted with a dashed line.

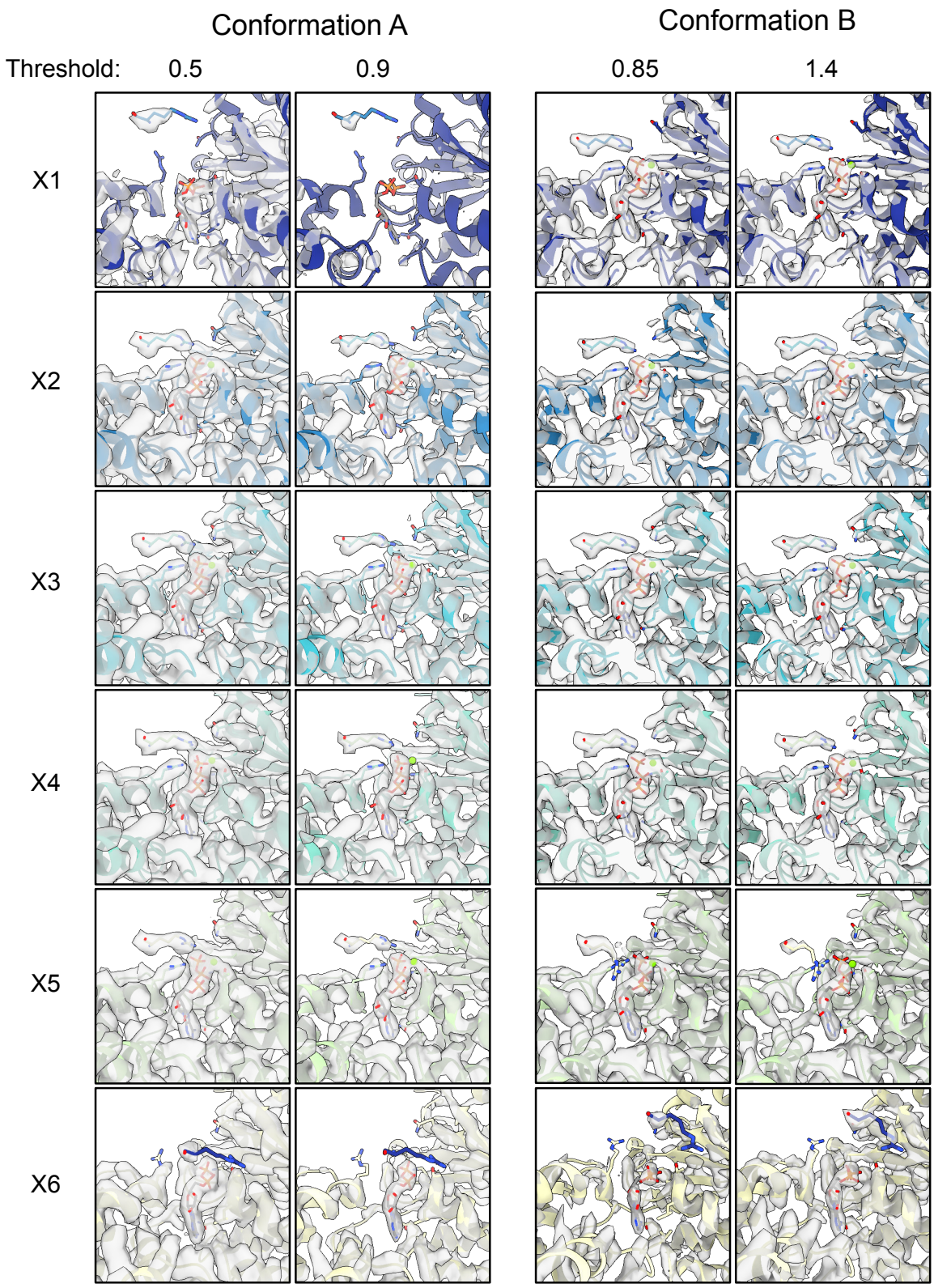

Figure 4 – Figure Supplement 3. ATP binding pocket densities. Experimental density maps and models are shown for the ATP binding pockets of all protomers. Two numerical thresholds are shown to highlight differences in density.

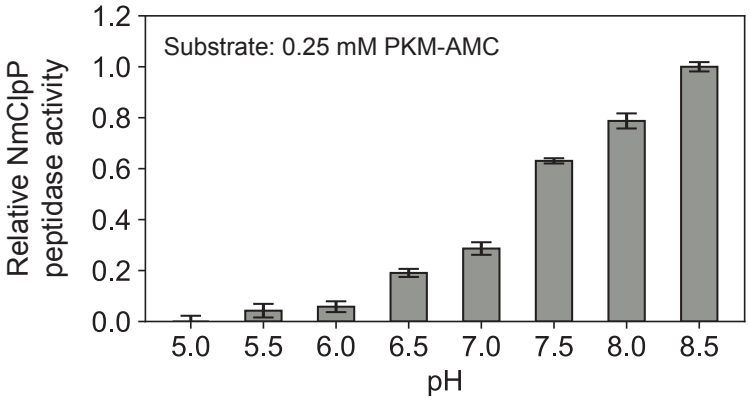

570
571 **Appendix Figure 1.** Peptidase rate measurements of NmClpP as a function of pH, monitored using the fluorogenic
572 substrate PKM-AMC.

573 **Video 1. Overview of the substrate bound ClpXP complex (Conformation B).**

574 **Video 2. Hand-over-hand translocation cycle of the ClpXP complex.** Interpolation between
575 states A → B → A → B. Side and top views of the complex are shown (top), along with the
576 pore-1 loop Tyr153 and substrate (bottom left) as well as IGF loops (bottom right).

577 **Video 3. ClpX precession on the ClpP apical surface.** Repeated interpolation between states
578 reveals a precession of the ClpX ring as its IGF loops are placed successively in different ClpP
579 binding sites. The position of the empty binding pocket on ClpP undergoes a complete cycle
580 around the complex for every 60º rotation of the ClpX ring relative to the ClpP ring.

581

582 **Supplementary File 1.** Cryo-EM data acquisition, processing, model statistics, and data
583 deposition. (A) CryoEM data acquisition and image processing. (B) Map and Model statistics.
584 (C) Residues excluded in atomic models. (D) Deposited maps and associated coordinate files.

585

586 **Materials and Methods:**

587 ***Plasmids and constructs*** Codon-optimized genes encoding NmClpX (Uniprot entry: Q9JYY3)
588 bearing an N-terminal His_6-TEV affinity tag and ClpP (Uniprot entry: Q9JZ38) with an N-
589 terminal His_6-SUMO tag were synthesized by GenScript (Piscataway, NJ, USA) and cloned into
590 the NdeI and BamHI sites of pET28a+ (Novagen, Madison, WI, USA). Point mutations were
591 introduced with the Quikchange mutagenesis method (Agilent, Santa Clara, CA, USA).

592 ***Expression and purification of NmClpP and NmClpX*** Transformed Codon+ *E. coli* BL21(DE3)
593 cells were grown in LB media at 37 °C. Protein over-expression was induced by addition of 0.2
594 mM IPTG at OD_{600}=1.0 and was allowed to proceed overnight at 18 °C. Cells were lysed in
595 buffer containing 50 mM Tris, 300 KCl, 10 mM imidazole, 10% glycerol, pH 7.0 and NmClpP

596 and NmClpX proteins purified by Ni-affinity chromatography [HisTrap HP (GE)] in lysis buffer.
597 Bound proteins were eluted from the Ni column by increasing the imidazole concentration to 500
598 mM. The affinity tag was removed by the addition of TEV (for ClpX) or Ulp1 (for ClpP)
599 protease followed by dialysis against lysis/wash buffer that included 5 mM DTT. Following a
600 reverse Ni-affinity chromatography step, the flow-through, free from the cleaved tag and other
601 impurities, was concentrated with an Amicon Ultra-15 50K MWCO (Millipore) concentrator and
602 subjected to size exclusion chromatography (SEC) with a Superdex 200 Increase 10/300 (GE)
603 column in SEC buffer (50 mM imidazole, 100 mM KCl, 5 mM DTT, pH 7.0). Fractions
604 corresponding to NmClpX and NmClpP were pooled and stored at 4 °C in the SEC buffer until
605 further use. Salts containing magnesium were avoided during the purification of NmClpX to
606 prevent protein aggregation. Protein concentrations were determined in 8 M GdnCl using
607 extinction coefficient values (7450 M^{-1} cm^{-1} for ClpP, 8940 M^{-1} cm^{-1} for ClpX) determined with
608 ExPASy's ProtParam (73).
609 ***Expression and purification of GFP-SsrA.*** Green fluorescent protein (GFP) bearing an 11-
610 residue SsrA degradation tag at its carboxyl terminus and a non-cleavable N-terminal His×6 tag
611 was purified by Ni affinity chromatography followed by SEC on a HiLoad 16/60 Superdex 75 pg
612 column (GE).
613 ***Peptidase rate measurements of NmClpP as a function of pH.*** The peptidase activity of
614 NmClpP was measured at 37 ºC with Acetyl-L-Pro-L-Lys-L-Met bearing a C-terminal
615 fluorogenic 7-amino-4-methylcoumarin group (PKM-AMC) as substrate. The reaction was
616 followed with a Synergy Neo2 96-well microplate reader making a measurement every 21
617 seconds for 60 minutes at λ_{ex}: 355 nm, λ_{em}: 460 nm. Each well contained 1 μM NmClpP
618 (monomer concentration), 250 μM PKM-AMC, 50 mM citrate, 50 mM phosphate, 50 mM Tris,

619 100 mM KCl in a total volume of 100 μL adjusted to the appropriate pH. Activities are derived
620 from initial rates extracted and analyzed using a python script written in-house. Standard errors
621 are calculated from repeating each reaction in triplicate.

622 ***GFP-SsrA degradation assays.*** Degradation of 1 μM samples of GFP-SsrA was followed by the
623 loss of GFP fluorescence (λ_{ex}: 480 nm, λ_{em}: 508 nm) with a Synergy Neo2 96-well microplate
624 reader at 25 °C. The wells included an ATP-regeneration system (74) that contained 1.5 mM
625 phosphoenolpyruvate, 0.2 mM NADH, 40 μg/mL pyruvate kinase, 40 μg/mL lactate
626 dehydrogenase, and 2 mM MgATP at pH 8.2. In some assays solutions also contained WT
627 NmClpX at 0.5 μM (hexamer) and/or WT ClpP at a 0.25 μM (tetradecamer), as indicated in
628 Figure 1B. All assays were performed in triplicate.

629 For the mixed protomer ClpX assays, WT ClpX and E185Q ClpX samples were purified
630 separately as described above (i.e. without the addition of any nucleotide) and mixed at the
631 indicated ratios. The mixture was left overnight for protomer exchange at room temperature
632 before being assayed for GFP unfolding and degradation as described. The addition of GdnCl to
633 promote protomer exchange is not necessary in this case because ClpX is not a stable hexamer in
634 the absence of nucleotide.

635 ***ATP hydrolysis assays:*** Steady state ATP hydrolysis was measured with an enzyme coupled
636 assay as described previously (74). The wells included an ATP-regeneration system that
637 contained 1.5 mM phosphoenolpyruvate, 0.2 mM NADH, 40 μg/mL pyruvate kinase, 40 μg/mL
638 lactate dehydrogenase, and 2 mM MgATP at pH 8.2. Hydrolysis of ATP was monitored by loss
639 of absorption at 340 nm with a Synergy Neo2 96-well microplate reader at 25 °C.

640 ***Preparation of samples for cryo-EM.*** A 1 mL mixture containing 10 μM (tetradecamer)
641 NmClpP and 20 μM NmClpX together with 200 μM GFP-SsrA was incubated with 20 mM

642 MgATP for 10 minutes at room temperature. This mixture was applied to a Superdex 200
643 Increase 10/300 (GE) column equilibrated with 50 mM bicine, 100 mM KCl, 2 mM MgATP, pH
644 adjusted to 8.2 at room temperature (equivalent to pH 8.5 at 4 °C – see Appendix Figure 1), as
645 the running buffer. Following SEC, a 0.5 mL fraction (denoted with a * in Figure 1 – Figure
646 Supplement 1) containing doubly capped ClpXP bound to GFP-SsrA was supplemented with 20
647 μM GFP-SsrA and vitrified immediately without the addition of any cross-linking agent or
648 detergent.

649 ***Sample vitrification.*** 2.5 μL of the sample mixtures were applied to nanofabricated holey gold
650 grids (75–77) with a hole size of ~1 μm, that had been glow discharged in air for 15 seconds.
651 Grids were blotted on both sides using a FEI Vitrobot mark III for 15 seconds at 4 °C and ~100%
652 relative humidity before freezing in a liquid ethane/propane mixture (78).

653 ***Electron Microscopy:*** NmClpXP was imaged with a Thermo Fisher Scientific Titan Krios G3
654 microscope operating at 300 kV and equipped with a FEI Falcon III DDD camera. Structures
655 were calculated from counting mode movies consisting of 30 frames, obtained over a 60 second
656 exposure with defocuses ranging from 0.9 to 1.7 μm. Movies were at a nominal magnification of
657 75000× corresponding to a calibrated pixel size of 1.06 Å and with an exposure of 0.8
658 electrons/pixel/s, giving a total exposure of 43 electrons/Å^2. 2680 movies were collected using
659 the microscope's *EPU* software. The Apo-NmClpP structure (with no ClpX or GFP present) was
660 calculated from data obtained using a FEI Tecnai F20 electron microscope operating at 200 kV
661 and equipped with a Gatan K2 Summit direct detector device camera. Movies consisting of 30
662 frames over a 15 second exposure were obtained with defocuses ranging from 1.7 to 2.9 μm.
663 Movies were collected in counting mode at a nominal magnification of 25000× corresponding to

664 a calibrated pixel size of 1.45 Å and with an exposure of 5 electrons/pixel/s, and a total exposure
665 of 35 electrons/Å^2. 122 movies were collected using Digital Micrograph software.
666 ***EM image analysis:*** Patch based whole frame alignment and exposure weighting was performed
667 in *cryoSPARC* v2 (55) with a 10×10 grid and the resulting averages of frames were used for
668 patch based contrast transfer function (CTF) determination. Templates for particle selection were
669 generated by 2D classification of manually selected particles. Particle images were extracted in
670 300×300-pixel boxes for further analysis. *Ab inito* map calculation was performed on a random
671 subset of 30,000 particle images, generating an initial map showing density for the complex of a
672 ClpP tetradecamer bound to two ClpX hexamers. A single round of 2D classification was used to
673 remove images of damaged particles and other contaminants from a dataset of 466,549 particle
674 images, with selected classes leaving 377,234 particle images for further analysis. Homogeneous
675 refinement of these particle images using D7 symmetry yielded a map of the complex, with good
676 density for only the ClpP portion, at 2.3 Å resolution.
677 To improve the density of the ClpX portion of the map, a round of *Ab initio* classification
678 was performed using three classes, of which two classes containing 289,144 particle images had
679 good density for ClpX, with the remaining class containing mostly density for ClpP. Refinement
680 of these particle images with C1 symmetry resulted in a map of the ClpXP complex at a nominal
681 resolution of 2.8 Å, but with poorly defined density for much of ClpX. To improve the
682 interpretability of the map in the ClpX region, local refinement was performed with a mask
683 around the six ClpX subunits without performing signal subtraction for ClpP. This refinement
684 greatly improved the map in the ClpX region, while blurring the density at the distal ClpP ring
685 (indicative of flexibility between ClpX and ClpP). However, density for two of the ClpX
686 subunits remained fragmented and at lower resolution. To help resolve the heterogeneity of this

687 region "3D variability analysis" was performed, which utilizes principle component analysis to
688 separate conformations. Clustering was performed along three eigenvectors. Two clusters were
689 identified along a single eigenvector corresponding to two conformations of ClpX bound to
690 substrate. From the trajectory identified, the two endpoints were used to seed a heterogeneous
691 classification in which the O-EM learning rate was reduced 10-fold to preserve the original
692 character of the seeds yielding two classes split ~ 40%:60% with 110,696 and 178,448 particle
693 images for Conformations A and B respectively. Subsequent non-uniform refinement yielded
694 maps at 3.3 Å and 2.9 Å respectively, which were then used for model building.

695 For Apo-NmClpP the same preprocessing steps were applied as described above, and
696 100,132 particle images were extracted in 160×160-pixel boxes for further analysis. Rounds of
697 2D classification and *ab initio* classification led to a subset of 50,400 particle images that were
698 used to refined a map to 4.1 Å resolution.

699 ***Atomic Model Building and Refinement:*** To model NmClpP, the crystal structure of NmClpP
700 (PDBID: 5DKP) (56) was rigidly fit with UCSF Chimera (79) into the 2.3 Å D7 symmetric map,
701 followed by relaxation with Rosetta using the density map as an additional term in the scoring
702 function (80), and utilizing D7 non crystallographic symmetry. The best scoring model was then
703 rigidly fit into the C1 symmetry focussed maps for Conformation A and B. Visual inspection and
704 real space refinement in *Coot* (81) was then used to better fit the model into the density where it
705 deviated from the ideal symmetry version, specifically in areas where ClpX contacted ClpP, and
706 the apical loops (N-terminal β-hairpins).

707 For NmClpX, Phyre2 (82) was used to perform one-to-one threading onto the previous
708 crystal structure of ClpX from *E. coli* (PDBID 3HWS chain A) (48). A single chain was then
709 rigidly docked into the X3 position of the 2.9 Å map, and real space refinement and *Ab initio*

710 model building of regions that poorly fit the density, as well as for regions missing from the
711 homology model was performed in *Coot* (81). This model was then relaxed with Rosetta (80),
712 and rigidly fit into the density for the other five ClpX protomers. Iterative rounds of real space
713 refinement and *Ab initio* model building in *Coot* (81), relaxation in Rosetta (80), and real space
714 refinement in Phenix (83), were then used to create the final model. To model Conformation A,
715 the model for Conformation B was used as a starting point before iterative rounds of real space
716 refinement and *Ab initio* model building in *Coot*, relaxation in Rosetta, and real space refinement
717 in Phenix. While the experimental density for the substrate showed some bulky side chains,
718 attempts to register the SsrA sequence in the density were unsuccessful and the substrate was
719 modeled as polyalanine. Models were evaluated with Molprobity (84) and EMRinger (85).
720 Figures and movies were generated in UCSF Chimera (79) and UCSF ChimeraX (86), and colors
721 chosen with ColorBrewer (87).
722

723 **Acknowledgements**

724 We thank Dr. Samir Benlekbir for cryo-EM data collection on the Titan Krios. ZAR and SV
725 were supported by a scholarship and a postdoctoral fellowship from the Canadian Institutes of
726 Health Research, respectively. LEK and JLR were supported by the Canada Research Chairs
727 program. This research was funded by Canadian Institutes of Health Research grants FDN-
728 503573 (LEK), PJT-162186 (JLR), and PJT-148564 (WAH). Titan Krios cryo-EM data were
729 collected at the Toronto High-Resolution High-Throughput cryo-EM facility supported by the
730 Canadian Foundation for Innovation and Ontario Research Fund.
731

732 **References:**

733 1. A. O. Olivares, T. A. Baker, R. T. Sauer, Mechanistic insights into bacterial AAA+
734 proteases and protein-remodelling machines. *Nat. Rev. Microbiol.* **14**, 33–44 (2016).
735 2. A. L. Goldberg, Protein degradation and protection against misfolded or damaged
736 proteins. *Nature* **426**, 895–899 (2003).
737 3. D. Frees, U. Gerth, H. Ingmer, Clp chaperones and proteases are central in stress survival,
738 virulence and antibiotic resistance of Staphylococcus aureus. *Int. J. Med. Microbiol.* **304**,
739 142–149 (2014).
740 4. C. M. Pickart, R. E. Cohen, Proteasomes and their kin: proteases in the machine age. *Nat.*
741 *Rev. Mol. Cell Biol.* **5**, 177–187 (2004).
742 5. V. Bhandari, K. S. Wong, J. L. Zhou, M. F. Mabanglo, R. A. Batey, W. A. Houry, The
743 Role of ClpP Protease in Bacterial Pathogenesis and Human Diseases. *ACS Chem. Biol.*
744 **13**, 1413–1425 (2018).
745 6. T. A. Baker, R. T. Sauer, ClpXP, an ATP-powered unfolding and protein-degradation
746 machine. *Biochim. Biophys. Acta* **1823**, 15–28 (2012).
747 7. T. Böttcher, S. A. Sieber, β-Lactones as Privileged Structures for the Active-Site Labeling
748 of Versatile Bacterial Enzyme Classes. *Angew. Chem. Int. Ed.* **47**, 4600–4603 (2008).
749 8. M. W. Hackl, M. Lakemeyer, M. Dahmen, M. Glaser, A. Pahl, K. Lorenz-Baath, T.
750 Menzel, S. Sievers, T. Böttcher, I. Antes, H. Waldmann, S. A. Sieber, Phenyl Esters Are
751 Potent Inhibitors of Caseinolytic Protease P and Reveal a Stereogenic Switch for
752 Deoligomerization. *J. Am. Chem. Soc.* **137**, 8475–8483 (2015).
753 9. M. Lakemeyer, E. Bertosin, F. Möller, D. Balogh, R. Strasser, H. Dietz, S. A. Sieber,
754 Tailored peptide phenyl esters block ClpXP proteolysis by an unusual breakdown into a
755 heptamer-hexamer assembly. *Angew. Chemie Int. Ed.* **0** (2019).

756 10. W. Gao, *et al.*, The Cyclic Peptide Ecumicin Targeting ClpC1 Is Active
757 againstMycobacterium tuberculosis In Vivo. *Antimicrob. Agents Chemother.* **59**, 880
758 (2015).
759 11. E. Gavrish, *et al.*, Lassomycin, a Ribosomally Synthesized Cyclic Peptide, Kills
760 Mycobacterium tuberculosis by Targeting the ATP-Dependent Protease ClpC1P1P2.
761 *Chem. Biol.* **21**, 509–518 (2014).
762 12. M. P. Choules, *et al.*, Rufomycin Targets ClpC1 Proteolysis in Mycobacterium
763 tuberculosis and M. abscessus. *Antimicrob. Agents Chemother.* **63**, e02204-18 (2019).
764 13. C. Fetzer, V. S. Korotkov, R. Thänert, K. M. Lee, M. Neuenschwander, J. P. von Kries, E.
765 Medina, S. A. Sieber, A Chemical Disruptor of the ClpX Chaperone Complex Attenuates
766 the Virulence of Multidrug-Resistant Staphylococcus aureus. *Angew. Chemie Int. Ed.* **56**,
767 15746–15750 (2017).
768 14. J. Kirstein, A. Hoffmann, H. Lilie, R. Schmidt, H. Rübsamen-Waigmann, H. Brötz-
769 Oesterhelt, A. Mogk, K. Turgay, The antibiotic ADEP reprogrammes ClpP, switching it
770 from a regulated to an uncontrolled protease. *EMBO Mol. Med.* **1**, 37–49 (2009).
771 15. M. Gersch, K. Famulla, M. Dahmen, C. Göbl, I. Malik, K. Richter, V. S. Korotkov, P.
772 Sass, H. Rübsamen-Schaeff, T. Madl, H. Brötz-Oesterhelt, S. A. Sieber, AAA+
773 chaperones and acyldepsipeptides activate the ClpP protease via conformational control.
774 *Nat. Commun.* **6**, 6320 (2015).
775 16. K. S. Wong, *et al.*, Acyldepsipeptide Analogs Dysregulate Human Mitochondrial ClpP
776 Protease Activity and Cause Apoptotic Cell Death. *Cell Chem. Biol.* **25**, 1017–1030.e9
777 (2018).
778 17. E. Culp, G. D. Wright, Bacterial proteases, untapped antimicrobial drug targets. *J.*

Antibiot. (Tokyo). **70**, 366–377 (2017).

18. I. T. Malik, H. Brotz-Oesterhelt, Conformational control of the bacterial Clp protease by natural product antibiotics. *Nat. Prod. Rep* **34**, 815–831 (2017).

19. R. M. Raju, A. L. Goldberg, E. J. Rubin, Bacterial proteolytic complexes as therapeutic targets. *Nat. Rev. Drug Discov.* **11**, 777–789 (2012).

20. C. A. Goard, A. D. Schimmer, Mitochondrial matrix proteases as novel therapeutic targets in malignancy. *Oncogene* **33**, 2690 (2013).

21. K. S. Wong, W. A. Houry, "Recent Advances in Targeting Human Mitochondrial AAA+ Proteases to Develop Novel Cancer Therapeutics" in *Mitochondria in Health and in Sickness*, A. Urbani, M. Babu, Eds. (Springer Singapore, 2019), pp. 119–142.

22. J. Wang, J. A. Hartling, J. M. Flanagan, The Structure of ClpP at 2.3 A° Resolution Suggests a Model for ATP-Dependent Proteolysis. *Cell* **91**, 447–456 (1997).

23. K. Liu, A. Ologbenla, W. A. Houry, Dynamics of the ClpP serine protease: A model for self-compartmentalized proteases. *Crit. Rev. Biochem. Mol. Biol.* **49**, 400–412 (2014).

24. F. Förster, P. Unverdorben, P. Śledź, W. Baumeister, Unveiling the Long-Held Secrets of the 26S Proteasome. *Structure* **21**, 1551–1562 (2013).

25. E. Kish-Trier, C. P. Hill, Structural Biology of the Proteasome. *Annu. Rev. Biophys.* **42**, 29–49 (2013).

26. J. Ortega, H. S. Lee, M. R. Maurizi, A. C. Steven, Alternating translocation of protein substrates from both ends of ClpXP protease. *EMBO J.* **21**, 4938–4949 (2002).

27. J. Ortega, S. K. Singh, T. Ishikawa, M. R. Maurizi, A. C. Steven, Visualization of Substrate Binding and Translocation by the ATP-Dependent Protease, ClpXP. *Mol. Cell* **6**, 1515–1521 (2000).

802 28. M. Kessel, M. R. Maurizi, B. Kim, E. Kocsis, B. L. Trus, S. K. Singh, A. C. Steven,
803 Homology in Structural Organization Between E. coli ClpAP Protease and the Eukaryotic
804 26 S Proteasome. *J. Mol. Biol.* **250**, 587–594 (1995).
805 29. M. E. Lee, T. A. Baker, R. T. Sauer, Control of Substrate Gating and Translocation into
806 ClpP by Channel Residues and ClpX Binding. *J. Mol. Biol.* **399**, 707–718 (2010).
807 30. D. H. S. Li, Y. S. Chung, M. Gloyd, E. Joseph, R. Ghirlando, G. D. Wright, Y. Q. Cheng,
808 M. R. Maurizi, A. Guarne, J. Ortega, Acyldepsipeptide Antibiotics Induce the Formation
809 of a Structured Axial Channel in ClpP: A Model for the ClpX/ClpA-Bound State of ClpP.
810 *Chem. Biol.* **17**, 959–969 (2010).
811 31. G. Effantin, M. R. Maurizi, A. C. Steven, Binding of the ClpA Unfoldase Opens the Axial
812 Gate of ClpP Peptidase. *J. Biol. Chem.* **285**, 14834–14840 (2010).
813 32. Y.-I. Kim, I. Levchenko, K. Fraczkowska, R. V Woodruff, R. T. Sauer, T. A. Baker,
814 Molecular determinants of complex formation between Clp/Hsp100 ATPases and the
815 ClpP peptidase. *Nat. Struct. Biol.* **8**, 230–233 (2001).
816 33. S. A. Joshi, G. L. Hersch, T. A. Baker, R. T. Sauer, Communication between ClpX and
817 ClpP during substrate processing and degradation. *Nat Struct Mol Biol* **11**, 404–411
818 (2004).
819 34. A. J. Amor, K. R. Schmitz, T. A. Baker, R. T. Sauer, Roles of the ClpX IGF loops in ClpP
820 association, dissociation, and protein degradation. *Protein Sci.* **28**, 756–765 (2019).
821 35. A. Gribun, M. S. Kimber, R. Ching, R. Sprangers, K. M. Fiebig, W. A. Houry, The ClpP
822 Double Ring Tetradecameric Protease Exhibits Plastic Ring-Ring Interactions, and the N
823 Termini of Its Subunits Form Flexible Loops That Are Essential for ClpXP and ClpAP
824 Complex Formation. *J. Bio. Chem.* **280**, 16185–16196 (2005).

825 36. L. D. Jennings, J. Bohon, M. R. Chance, S. Licht, The ClpP N-Terminus Coordinates
826 Substrate Access with Protease Active Site Reactivity. *Biochemistry* **47**, 11031–11040
827 (2008).
828 37. A. Martin, T. A. Baker, R. T. Sauer, Diverse Pore Loops of the AAA+ ClpX Machine
829 Mediate Unassisted and Adaptor-Dependent Recognition of ssrA-Tagged Substrates. *Mol.*
830 *Cell* **29**, 441–450 (2008).
831 38. A. Martin, T. A. Baker, R. T. Sauer, Pore loops of the AAA+ ClpX machine grip
832 substrates to drive translocation and unfolding. *Nat Struct Mol Biol* **15**, 1147–1151 (2008).
833 39. N. Monroe, H. Han, P. S. Shen, W. I. Sundquist, C. P. Hill, Structural basis of protein
834 translocation by the Vps4-Vta1 AAA ATPase. *Elife* **6** (2017).
835 40. H. Yu, T. J. Lupoli, A. Kovach, X. Meng, G. Zhao, C. F. Nathan, H. Li, ATP hydrolysis-
836 coupled peptide translocation mechanism of Mycobacterium tuberculosis ClpB. *Proc.*
837 *Natl. Acad. Sci. U. S. A.* **115**, E9560–E9569 (2018).
838 41. A. H. De la Peña, E. A. Goodall, S. N. Gates, G. C. Lander, A. Martin, Substrate-engaged
839 26S proteasome structures reveal mechanisms for ATP-hydrolysis–driven translocation.
840 *Science (80-.).* **362**, eaav0725 (2018).
841 42. M. Shin, A. Asmita, C. Puchades, E. Adjei, R. L. Wiseman, A. W. Karzai, G. C. Lander,
842 Distinct Structural Features of the Lon Protease Drive Conserved Hand-over-Hand
843 Substrate Translocation. *bioRxiv*, 617159 (2019).
844 43. Z. A. Ripstein, R. Huang, R. Augustyniak, L. E. Kay, J. L. Rubinstein, Structure of a
845 AAA+ unfoldase in the process of unfolding substrate. *Elife* **6**, e25754 (2017).
846 44. S. N. Gates, *et al.*, Ratchet-like polypeptide translocation mechanism of the AAA +
847 disaggregase Hsp104. **1052**, 1–13 (2017).

848 45. M. Li, O. Kandror, T. Akopian, P. Dharkar, A. Wlodawer, M. R. Maurizi, A. L. Goldberg,
849 Structure and Functional Properties of the Active Form of the Proteolytic Complex,
850 ClpP1P2, from Mycobacterium tuberculosis. *J. Biol. Chem.* **291**, 7465–7476 (2016).
851 46. S. R. Geiger, T. Bottcher, S. A. Sieber, P. Cramer, A Conformational Switch Underlies
852 ClpP Protease Function. *Angew. Chem. Int. Ed.* **50**, 5749–5752 (2011).
853 47. J. Ishizawa, *et al.*, Mitochondrial ClpP-Mediated Proteolysis Induces Selective Cancer
854 Cell Lethality. *Cancer Cell* (2019)
855 https:/doi.org/https://doi.org/10.1016/j.ccell.2019.03.014.
856 48. S. E. Glynn, A. Martin, A. R. Nager, T. A. Baker, R. T. Sauer, Structures of Asymmetric
857 ClpX Hexamers Reveal Nucleotide-Dependent Motions in a AAA+ Protein-Unfolding
858 Machine. *Cell* **139**, 744–756 (2007).
859 49. M. C. Bewley, V. Graziano, K. Griffin, J. M. Flanagan, The asymmetry in the mature
860 amino-terminus of ClpP facilitates a local symmetry match in ClpAP and ClpXP
861 complexes. *J. Struct. Biol.* **153**, 113–128 (2006).
862 50. F. Beuron, M. R. Maurizi, D. M. Belnap, E. Kocsis, F. P. Booy, M. Kessel, A. C. Steven,
863 At Sixes and Sevens: Characterization of the Symmetry Mismatch of the ClpAP
864 Chaperone-Assisted Protease. *J. Mol. Biol.* **123**, 248–259 (1998).
865 51. P. Majumder, T. Rudack, F. Beck, R. Danev, G. Pfeifer, I. Nagy, W. Baumeister, Cryo-
866 EM structures of the archaeal PAN-proteasome reveal an around-the-ring ATPase cycle.
867 *Proc. Natl. Acad. Sci.* **116**, 534 LP-539 (2019).
868 52. G. L. Hersch, R. E. Burton, D. N. Bolon, T. A. Baker, R. T. Sauer, Asymmetric
869 Interactions of ATP with the AAA+ ClpX6 Unfoldase: Allosteric Control of a Protein
870 Machine. *Cell* **121**, 1017–1027 (2005).

871 53. R. Grimaud, M. Kessel, F. Beuron, A. C. Steven, M. R. Maurizi, Enzymatic and Structural
872 Similarities between theEscherichia coli ATP-dependent Proteases, ClpXP and ClpAP. *J.*
873 *Biol. Chem.* **273**, 12476–12481 (1998).
874 54. J. M. Jones, D. J. Welty, H. Nakai, Versatile Action of Escherichia coli ClpXP as Protease
875 or Molecular Chaperone for Bacteriophage Mu Transposition. *J. Biol. Chem.* **273**, 459–
876 465 (1998).
877 55. A. Punjani, J. L. Rubinstein, D. J. Fleet, M. A. Brubaker, cryoSPARC: algorithms for
878 rapid unsupervised cryo-EM structure determination. *Nat. Methods* **14**, 290–+ (2017).
879 56. J. D. Goodreid, J. Janetzko, J. P. Santa Maria, K. S. Wong, E. Leung, B. T. Eger, S.
880 Bryson, E. F. Pai, S. D. Gray-Owen, S. Walker, W. A. Houry, R. A. Batey, Development
881 and Characterization of Potent Cyclic Acyldepsipeptide Analogues with Increased
882 Antimicrobial Activity. *J. Med. Chem.* **59**, 624–646 (2016).
883 57. A. Martin, T. A. Baker, R. T. Sauer, Distinct static and dynamic interactions control
884 ATPase-Peptidase communication in a AAA plus protease. *Mol. Cell* **27**, 41–52 (2007).
885 58. J. Ortega, H. S. Lee, M. R. Maurizi, A. C. Steven, ClpA and ClpX ATPases bind
886 simultaneously to opposite ends of ClpP peptidase to form active hybrid complexes. *J.*
887 *Struct. Biol.* **146**, 217–226 (2004).
888 59. S. K. Singh, R. Grimaud, J. R. Hoskins, S. Wickner, M. R. Maurizi, Unfolding and
889 internalization of proteins by the ATP-dependent proteases ClpXP and ClpAP. *Proc. Natl.*
890 *Acad. Sci.* **97**, 8898 LP-8903 (2000).
891 60. A. Martin, T. A. Baker, R. T. Sauer, Distinct Static and Dynamic Interactions Control
892 ATPase-Peptidase Communication in a AAA+ Protease. *Mol. Cell* **27**, 41–52 (2007).
893 61. C. M. Farrell, T. A. Baker, R. T. Sauer, Altered Specificity of a AAA+ Protease. *Mol. Cell*

894 **25**, 161–166 (2007).

895 62. S. M. Siddiqui, R. T. Sauer, T. A. Baker, Role of the processing pore of the ClpX AAA+
896 ATPase in the recognition and engagement of specific protein substrates. *Genes Dev.* **18**,
897 369–374 (2004).

898 63. A. Martin, T. A. Baker, R. T. Sauer, Rebuilt AAA + motors reveal operating principles for
899 ATP-fuelled machines. *Nature* **437**, 1115–1120 (2005).

900 64. S. Vahidi, Z. A. Ripstein, M. Bonomi, T. Yuwen, M. F. Mabanglo, J. B. Juravsky, K.
901 Rizzolo, A. Velyvis, W. A. Houry, M. Vendruscolo, J. L. Rubinstein, L. E. Kay,
902 Reversible inhibition of the ClpP protease via an N-terminal conformational switch. *Proc.*
903 *Natl. Acad. Sci.* **115**, E6447--E6456 (2018).

904 65. R. Huang, F. Perez, L. E. Kay, Probing the cooperativity of Thermoplasma acidophilum
905 proteasome core particle gating by NMR spectroscopy. *Proc. Natl. Acad. Sci. U.S.A.* **114**,
906 E9846–E9854 (2017).

907 66. R. Augustyniak, L. E. Kay, Cotranslocational processing of the protein substrate
908 calmodulin by an AAA+ unfoldase occurs via unfolding and refolding intermediates.
909 *Proc. Natl. Acad. Sci.* **115**, E4786 LP-E4795 (2018).

910 67. C. Gatsogiannis, D. Balogh, F. Merino, S. A. Sieber, S. Raunser, Cryo-EM structure of the
911 ClpXP protein degradation machinery. *bioRxiv*, 638692 (2019).

912 68. X. Fei, T. A. Bell, S. Jenni, B. M. Stinson, T. A. Baker, S. C. Harrison, R. T. Sauer,
913 Structures of the ATP-fueled ClpXP proteolytic machine bound to protein substrate.
914 *bioRxiv*, 704999 (2019).

915 69. E. J. Enemark, L. Joshua-Tor, Mechanism of DNA translocation in a replicative
916 hexameric helicase. *Nature* **442**, 270–275 (2006).

917 70. R. Huang, Z. a Ripstein, R. Augustyniak, M. Lazniewski, K. Ginalski, L. E. Kay, J. L.
918 Rubinstein, Unfolding the mechanism of the AAA+ unfoldase VAT by a combined cryo-
919 EM, solution NMR study. *Proc. Natl. Acad. Sci. U. S. A.* (2016)
920 https:/doi.org/10.1073/pnas.1603980113.
921 71. K. E. Lopez, A. N. Rizo, E. Tse, J. Lin, N. W. Scull, A. C. Thwin, A. L. Lucius, J.
922 Shorter, D. R. Southworth, Conformational Plasticity of the ClpAP AAA+ Protease
923 Couples Protein Unfolding and Proteolysis. *bioRxiv* (2019) https:/doi.org/10.1101/820209.
924 72. J. G. Nørby, Coupled assay of Na+,K+-ATPase activity. *Methods Enzymol.* **156**, 116–9
925 (1988).
926 73. E. Gasteiger, C. Hoogland, A. Gattiker, S. Duvaud, M. R. Wilkins, R. D. Appel, A.
927 Bairoch, "Protein Identification and Analysis Tools on the ExPASy Server" in *The*
928 *Proteomics Protocols Handbook*, J. M. Walker, Ed. (Humana Press, 2005), pp. 571–607.
929 74. J. G. B. T.-M. in E. Nørby, "[11] Coupled assay of Na+,K+-ATPase activity" in
930 *Biomembranes Part P: ATP-Driven Pumps and Related Transport: The Na,K-Pump*,
931 (Academic Press, 1988), pp. 116–119.
932 75. C. R. Marr, S. Benlekbir, J. L. Rubinstein, Fabrication of carbon films with ~500nm holes
933 for cryo-EM with a direct detector device. *J. Struct. Biol.* **185**, 42–47 (2014).
934 76. C. J. Russo, L. A. Passmore, Ultrastable gold subtrates for electron cryomicroscopy.
935 *Science (80-.).* **346**, 1377–1380 (2014).
936 77. J. R. Meyerson, P. Rao, J. Kumar, S. Chittori, S. Banerjee, J. Pierson, M. L. Mayer, S.
937 Subramaniam, Self-assembled monolayers improve protein distribution on holey carbon
938 cryo-EM supports. *Sci. Rep.* **4**, 7084 (2014).
939 78. W. F. Tivol, A. Briegel, G. J. Jensen, An improved cryogen for plunge freezing. *Microsc.*

940 *Microanal.* **14**, 375–379 (2008).

941 79. E. F. Pettersen, T. D. Goddard, C. C. Huang, G. S. Couch, D. M. Greenblatt, E. C. Meng,
942 T. E. Ferrin, UCSF Chimera—A visualization system for exploratory research and
943 analysis. *J. Comput. Chem.* **25**, 1605–1612 (2004).

944 80. R. Y. R. Wang, M. Kudryashev, X. Li, E. H. Egelman, M. Basler, Y. Cheng, D. Baker, F.
945 Dimaio, De novo protein structure determination from near-atomic-resolution cryo-EM
946 maps. *Nat. Methods* **12**, 335–338 (2015).

947 81. P. Emsley, K. Cowtan, Coot: model-building tools for molecular graphics. *Acta*
948 *Crystallogr. Sect. D* **60**, 2126–2132 (2004).

949 82. L. A. Kelley, S. Mezulis, C. M. Yates, M. N. Wass, M. J. E. Sternberg, The Phyre2 web
950 portal for protein modeling, prediction and analysis. *Nat. Protoc.* **10**, 845 (2015).

951 83. P. D. Adams, *et al.*, PHENIX: a comprehensive Python-based system for macromolecular
952 structure solution. *Acta Crystallogr. Sect. D* **66**, 213–221 (2010).

953 84. V. B. Chen, W. B. Arendall III, J. J. Headd, D. A. Keedy, R. M. Immormino, G. J. Kapral,
954 L. W. Murray, J. S. Richardson, D. C. Richardson, MolProbity: all-atom structure
955 validation for macromolecular crystallography. *Acta Crystallogr. Sect. D* **66**, 12–21
956 (2010).

957 85. B. A. Barad, N. Echols, R. Y.-R. Wang, Y. Cheng, F. DiMaio, P. D. Adams, J. S. Fraser,
958 EMRinger: side chain–directed model and map validation for 3D cryo-electron
959 microscopy. *Nat. Methods* **12**, 943 (2015).

960 86. T. D. Goddard, C. C. Huang, E. C. Meng, E. F. Pettersen, G. S. Couch, J. H. Morris, T. E.
961 Ferrin, UCSF ChimeraX: Meeting modern challenges in visualization and analysis.
962 *Protein Sci.* **27**, 14–25 (2018).

87. M. Harrower, C. A. Brewer, ColorBrewer.org: An Online Tool for Selecting Colour Schemes for Maps. *Cartogr. J.* **40**, 27–37 (2003).